

# *Intensification variability of tropical cyclones in directional shear flows: vortex tilt-convection coupling*

Article

Accepted Version

Gu, J.-F. ORCID: <https://orcid.org/0000-0002-7752-4553>, Tan, Z.-M. and Qiu, X. (2019) Intensification variability of tropical cyclones in directional shear flows: vortex tilt-convection coupling. *Journal of the Atmospheric Sciences*, 76 (6). pp. 1827-1844. ISSN 1520-0469 doi: 10.1175/JAS-D-18-0282.1 Available at <https://centaur.reading.ac.uk/83797/>

It is advisable to refer to the publisher's version if you intend to cite from the work. See [Guidance on citing](#).

To link to this article DOI: <http://dx.doi.org/10.1175/JAS-D-18-0282.1>

Publisher: American Meteorological Society

All outputs in CentAUR are protected by Intellectual Property Rights law, including copyright law. Copyright and IPR is retained by the creators or other copyright holders. Terms and conditions for use of this material are defined in the [End User Agreement](#).

[www.reading.ac.uk/centaur](http://www.reading.ac.uk/centaur)

**CentAUR**

Central Archive at the University of Reading

Reading's research outputs online



# Intensification Variability of Tropical Cyclones in Directional Shear

## Flows: Vortex Tilt-Convection Coupling

Jian-Feng Gu<sup>1,2</sup>, Zhe-Min Tan<sup>1\*</sup> and Xin Qiu<sup>1</sup>

1. *Key Laboratory of Mesoscale Severe Weather/MOE, and*

*School of Atmospheric Sciences, Nanjing University, Nanjing, China*

2. *Department of Meteorology, University of Reading, Reading, United Kingdom*

Submitted to *Journal of the Atmospheric Sciences* for publication

September 16, 2018

Revised, February 9, 2019

Revised, April 27, 2019

*\*Corresponding author address: Zhe-Min Tan, School of Atmospheric Sciences*

*Nanjing University, Nanjing 210023, China*

*Email: [zmtan@nju.edu.cn](mailto:zmtan@nju.edu.cn)*

1

1

**Early Online Release:** This preliminary version has been accepted for publication in *Journal of the Atmospheric Sciences*, may be fully cited, and has been assigned DOI 10.1175/JAS-D-18-0282.1. The final typeset copyedited article will replace the EOR at the above DOI when it is published.

## Abstract

The coupling of vortex tilt and convection, and their effects on the intensification variability of tropical cyclones (TCs) in directional shear flows is investigated. The height-dependent vortex tilt controls TC structural differences in clockwise (CW) and counter-clockwise (CC) hodographs during their initial stage of development. Moist convection may enhance the coupling between displaced vortices at different levels and thus reduce the vortex tilt amplitude and enhance precession of the overall vortex tilt during the early stage of development. However, differences in the overall vortex tilt between CW and CC hodographs are further amplified by a feedback from convective heating and therefore result in much higher intensification rates for TCs in CW hodographs than in CC hodographs.

In CW hodographs, convection organization in the left-of-shear region is favored because the low-level vortex tilt is ahead of the overall vortex tilt and the TC moves to the left side of the deep-layer shear. This results in a more humid mid-troposphere and stronger surface heat flux on the left side (azimuthally downwind) of the overall vortex tilt, thus providing a positive feedback and supporting continuous precession of the vortex tilt into the up-shear-left region.

In CC hodographs, convection tends to organize in the right side (azimuthally upwind) of the overall vortex tilt because the low-level vortex tilt is behind the overall vortex tilt and the TC moves to the right side of the deep-layer shear. In addition, convection organizes radially outward near the down-shear-right region, which weakens convection within the inner region. These configurations lead to a drier mid-troposphere and weaker surface heat flux in the downwind region of the overall vortex tilt and also a broader potential vorticity skirt. As a result, a negative feedback is established that prevents continuous precession of the overall vortex tilt.

## 27 **1. Introduction**

28 Environmental directional shear flows that change wind direction with height  
29 can result in significant variability of the intensification rate of tropical cyclones (TCs).  
30 Tropical cyclones intensify more rapidly in clockwise (CW) hodographs than in  
31 counter-clockwise (CC) hodographs, even if the deep-layer shear between 200 and 850  
32 hPa is identical (Nolan 2011, hereafter N11). It is important to understand the physics  
33 that underlies the uncertainties of TC intensification in directional shear flows, as  
34 environmental flows in the real atmosphere are more complicated than idealized  
35 unidirectional shear flows (e.g. Wang et al. 2015).

36 Distinct TC structural features (e.g., local helicity, the position of convection,  
37 surface heat flux relative to the deep-layer shear) have been identified to be responsible  
38 for variations in convective heating and the precession of convection, thus leading to  
39 variability in TC intensification in directional shear flows (Onderlinde and Nolan 2014,  
40 2016; hereafter ON14, ON16). Recently, Gu et al. (2018, hereafter GTQ18) showed  
41 that TC structural differences in CW and CC hodographs are rooted in dry dynamics;  
42 i.e., they arise from a balanced response to distinct configurations of height-dependent  
43 vortex tilt in directional shear flows, particularly low-level vortex tilt relative to the  
44 overall vortex tilt. However, the extent to which vortex tilt-dominated dynamics can  
45 explain structural features in moist simulations remains unclear. For example, it is not  
46 obvious how dry dynamics could result in different surface heat-flux structures within  
47 the inner-core region of TCs.

48 The continuous advancement of convection into the up-shear region is an  
49 essential process in TC intensification in directional shear flows (Rappin and Nolan  
50 2012; ON14; Stevens et al. 2014; ON16; Rogers et al. 2016; Munsell et al. 2017; Chen  
51 et al. 2018). As proposed by GTQ18, low-level upward motion is more likely to be

52 triggered in the downwind region of overall vortex tilt in CW hodographs than in CC  
53 hodographs because the low-level vortex tilt is ahead of the overall vortex tilt in the  
54 former but behind the overall vortex tilt in the latter. As a result, differences in  
55 convection precession in directional shear flows may also originate from the position  
56 of low-level vortex tilt relative to the overall vortex tilt. In addition to vortex tilt-  
57 dominated dry dynamics, moist convection is important in amplifying the differences  
58 in the precession of the tilted vortex, which leads to differences in TC intensification.  
59 Using trajectory analyses, ON16 showed that air parcels experiencing larger surface  
60 heat fluxes in the up-shear region of CW hodographs can be more easily ingested into  
61 the TC core than CC hodographs. As a result, convection can more easily advance into  
62 the up-shear region in CW hodographs. In addition to surface heat flux, observations  
63 also emphasize the importance of favorable moist environments in the mid-troposphere  
64 and high sea-surface temperatures in supporting persistent deep convection in up-shear  
65 regions (Rogers et al. 2016; Zawislak et al. 2016).

66 In the real atmosphere, both dry and moist dynamics are expected to contribute  
67 to variations in TC intensification rates in directional shear flows. Frank and Ritchie  
68 (1999) found that, in the unidirectional shear, the asymmetric structures are controlled  
69 by the dry dynamics in response to the deep-layer shear and boundary layer  
70 convergence during the early stage of the simulation and later on are further changed  
71 by the moist dynamics. However, little is known about how the dry and moist processes  
72 are related and how they collectively affect TC intensity in different directional shear  
73 flows. In this study, we combine vortex tilt-dominated dry dynamics and moist  
74 processes together to develop a more complete understanding of distinct TC features  
75 and propose a pathway that couples various structures to result in the diverse evolution  
76 of TCs in directional shear flows. We will demonstrate that convective heating plays

77 an important role in coupling the distinct structures, and that the convective  
78 organization determines whether a positive or negative feedback for overall vortex tilt  
79 precession and TC intensification is established.

80 The remainder of this paper is organized as follows. Section 2 describes the  
81 numerical model and design of the experiments. Section 3 explains how the dry  
82 dynamics couples with moist convection to result in distinct structures in CW and CC  
83 hodographs. Section 4 examines the different organization of convection in CW and  
84 CC hodographs and discusses possible mechanisms. Section 5 presents details of how  
85 these structures cooperate together through convective heating to form vortex tilt  
86 precessions that are more favorable for TC intensification in CW than in CC  
87 hodographs. Moreover, the role of surface heat flux on overall vortex tilt precession is  
88 discussed. A comparison of results from this study with other modelling and  
89 observational studies is provided in section 6. Finally, section 7 gives a brief summary  
90 of the results.

91

## 92 **2. Model setup and simulation design**

93 Following the methodology of GTQ18, this study uses the Weather Research and  
94 Forecasting model Version 3.4 (WRFV3.4; Skamarock et al. 2008) with the point-  
95 downscaling (PDS) method (Nolan 2011) implemented to investigate vortex evolution  
96 in directional shear flows. We use the same domain, initial vortex, boundary conditions,  
97 and background directional shear flows as in GTQ18. Most model configurations also  
98 follow those of GTQ18 to allow a direct comparison of the results of moist simulations  
99 with those of the dry simulations in GTQ18. Readers can refer to GTQ18 for more  
100 details of the experiment setup. A two-way nesting is employed in all the simulations.  
101 The difference between GTQ18 and the present study is that moist convection is

102 included here. The surface sea temperature is fixed to be 30 °C. The WRF single-  
103 moment 6-class microphysics scheme (WSM6; Hong and Lim 2006) is used to simulate  
104 microphysical processes including graupel; no cumulus parameterization is applied.  
105 The Yonsei University PBL scheme (YSU; Hong et al. 2006) is used to parameterize  
106 vertical mixing in the planetary boundary layer. For simplicity, both the longwave and  
107 shortwave radiation are turned off. Our simulations do not employ nudging as in ON16  
108 since it is not possible to keep the environmental flow steady in the real atmosphere.

109         The hodograph of the background directional shear flow is shown in Fig. 1a.  
110 Seven control simulations, referred to as CW5, CW2.5, CW1.25, UNIDIR, CC1.25,  
111 CC2.5, and CC5, are performed, as in GTQ18. The UNIDIR simulation is a  
112 unidirectional shear flow simulation. The numbers represent the amplitude of the cosine  
113 function for meridional wind. The environmental  $u$  component has a cosine shape with  
114 easterly winds of  $5 \text{ m s}^{-1}$  below 850 hPa and a westerly flow of  $5 \text{ m s}^{-1}$  above 200 hPa  
115 in all the simulations. Therefore, the deep-layer shear between 200 and 850 hPa in all  
116 the simulations corresponds to a  $10 \text{ m s}^{-1}$  westerly shear flow.

117         In addition to these simulations, two sets of sensitivity experiments are  
118 conducted based on the simulation CW2.5. In the first set of sensitivity simulations,  
119 convective heating is suppressed to investigate its role in vortex tilt precession. In these  
120 simulations, labelled CW2.5\_0.5DH and CW2.5\_0DH, the amplitudes of latent heating  
121 in the microphysical processes are modified at each time step to be 0.5 and 0 times the  
122 original values before updating the temperature, respectively. In the second set of  
123 sensitivity experiments, labelled CW2.5\_0.5MSF and CW2.5\_0MSF, the strong  
124 surface heat flux (latent heat flux plus sensible heat flux) is removed at each time step  
125 to examine its role in the precession of vortex tilt into the up-shear region. In  
126 CW2.5\_0.5MSF, surface heat fluxes that are larger than half the maximum value across

127 the domain are set to zero. The maximum value is calculated within the innermost  
128 domain at every time step. As strong surface heat fluxes are primarily located in the  
129 downstream region of convection (see section 3 and Fig. 4), these sensitivity  
130 simulations only remove strong heat fluxes that are near the downwind region of  
131 convection clusters. In CW2.5\_0MSF, all surface heat fluxes across the inner-domain  
132 are removed. The suppression of convective heating and removal of strong surface heat  
133 fluxes are only applied across the innermost domain and between hours 15 and 25,  
134 during which the differences in the precession of overall vortex tilt lead to various TC  
135 intensification rates in CW and CC hodographs.

136

### 137 **3. Imprint of dry dynamics in the moist simulations**

138 The evolution of TC intensity in all the control simulations is similar during the  
139 first 20 hours (Fig. 1b). After hour 20, the TCs in the CW and UNIDIR hodographs  
140 begin to intensify rapidly, whereas TCs have a much slower intensification rate in  
141 CC1.25 and CC2.5 and undergo no intensification in CC5. This is consistent with  
142 previous studies (N11, ON14 and ON16), which found that CW hodographs are more  
143 favorable for TC intensification than CC hodographs. Structural differences and  
144 physical processes that occur around hour 20 are critical for various TC intensification  
145 rates. In the following section, two periods (from hour 15 to 20 and hour 20 to 25)  
146 during TC development are discussed in detail.

147 The evolution of overall vortex tilt before hour 15 confirms the importance of  
148 dry dynamics, as identified by GTQ18 (Fig. 2). Vortex centers are calculated as the  
149 vorticity centroid within a radius of 200 km from the location of minimum pressure at  
150 each level. At early stages (before hour 15), the magnitudes of overall vortex tilt all  
151 increase and do not differ significantly regardless of whether the directional shear flow

152 rotates clockwise or counter-clockwise (Fig. 2a). However, overall vortex tilts in CW  
153 hodographs are directed toward the down-shear-left region, compared with down-shear  
154 and down-shear-right regions in CC hodographs (Fig. 2b). These features are consistent  
155 with the results of GTQ18, which did not consider moist convection.

156 Differences in the distributions of convection within TCs in CW and CC  
157 hodographs exist prior to the development of differences in TC intensity (Fig. 3). At  
158 hour 15, convective clusters in CW hodographs are located in the down-shear-left  
159 (CW1.25 and CW2.5) or left-of-shear (CW5) regions (Figs. 3a–c), whereas those in CC  
160 hodographs are concentrated in the down-shear-right region (Figs. 3d–f). The locations  
161 of convective clusters are generally in-phase with the direction of overall vortex tilt. In  
162 contrast to ON14, no obvious displacement of local positive helicity from convection  
163 is found in our simulations (Fig. 3). Actually, the convection is also generally in phase  
164 with local positive helicity in ON14 (Fig. 9 in ON14). It is a direct manifestation of dry  
165 dynamics that upward motions are a balanced response to vortex tilt and are generally  
166 collocated with positive local helicity (GTQ18). In response to the vortex tilt, the  
167 isentropic surface must be distorted in the down-tilt direction and upward motion must  
168 occur to the right-of-tilt side along the isentropic surface. At the same time, the wind  
169 direction changes in a clockwise sense to the right-of-tilt side and thus the positive helicity  
170 is collocated with convection in the moist simulation. Theoretical studies show that the  
171 positive helicity indicates warm advection (Tan and Wu 1994) in the adiabatic flow and  
172 thus the vertical motion is proportional to the local helicity (Hide 2002). This also indicates  
173 the collocation of local helicity and convection. A detailed investigation shows that more  
174 convection is located ahead of the overall vortex tilt in CW hodographs than in CC  
175 hodographs. This is because the low-level vortex tilt in CW hodographs has a different  
176 configuration with respect to the overall vortex tilt than does that in CC hodographs, as  
177 explained by GTQ18. In CW5, low-level vortex tilt (2–5 km) is closer to the up-shear

178 region than the overall vortex tilt (Fig. 3c), but is closer to the right-of-shear region than  
179 the overall vortex tilt in CC5 (Fig. 3f). As a result of balanced dynamics, stronger  
180 upward motion occurs at low levels, leading to convection clusters that are ahead of the  
181 overall vortex tilt in CW5 hodographs. There are no obvious differences between  
182 overall vortex tilt and low-level vortex tilt in the other cases (Figs. 3a, b, d, and e). This  
183 is due to the enhanced coupling between vortex centers at different levels from the  
184 feedback of moist convection, and also the smaller curvature in directional shear flow  
185 than in CW5 and CC5.

186         Although the vortex tilt affects the location of convection during the early stage  
187 of TC development, it alone cannot capture all observed differences, such as the  
188 configuration of surface heat flux, which has been shown to be important for the  
189 precession of convection in directional shear flows (ON16). Figure 4 shows that strong  
190 surface heat flux (the sum of sensible and latent heat fluxes) is generally located  
191 between the up-shear-left region in CW2.5 and CW5 (Figs. 4b and c) and the left-of-  
192 shear region in CW1.25 (Fig. 4a), but is concentrated in the down-shear-left region in  
193 CC1.25 and CC2.5 (Figs. 4d and e) and the down-shear region in CC5 (Fig. 4f). The  
194 preference of strong surface heat fluxes to be located near the left-of-shear region can  
195 be explained by stronger surface wind speeds in this region due to the superposition of  
196 low-level flow with cyclonic circulation, as low-level environmental winds come from  
197 the east in all the simulations. In addition, the evolution of low-level winds in shear  
198 flows is also quadrant-dependent with stronger winds in the left-of-shear region (Gu et  
199 al. 2016). The relative locations of strong surface heat fluxes are consistent with the  
200 results of ON16. However, the strength of the surface heat flux at hour 15 in CW  
201 hodographs is weaker than that in CC hodographs. This is in contrast with ON16, who  
202 found that the surface heat flux is stronger in CW hodographs than in CC hodographs

203 before differences in TC intensification rates develop. Because the surface heat flux  
204 does not solely depend on the surface wind speed, it is also necessary to investigate the  
205 structure of thermodynamic disequilibrium, as the surface heat flux is the product of  
206 these two factors. Figure 4 shows that low equivalent potential temperatures generally  
207 overlap with strong surface heat flux. By examining a composite vertical cross-section  
208 along the line of strong surface heat flux and convection (not shown), we find that  
209 precipitation downdrafts that originate from convection bring mid-level low-entropy air  
210 into the boundary layer, building a cold reservoir and a region of large thermodynamic  
211 disequilibrium, resulting in strong surface heat fluxes in the downstream region of  
212 convective clusters in both CW and CC hodographs. Therefore, the stronger surface  
213 heat fluxes in CC hodographs before the intensification rates differ are primarily due to  
214 the stronger cold pool strength, which is further related with the strength of convection.  
215 During 15-20 h, the low entropy downdrafts are stronger in CC hodographs than in CW  
216 hodographs (not shown). The relative strength of surface heat fluxes between CW and  
217 CC hodographs will change during later hours, depending on the strength of convection  
218 within the inner core region (see section 4). It is not clear why the convective strength are  
219 different in CC and CW hodographs during different time periods and deserves more  
220 detailed investigation in the future. Please note that the comparison of surface heat fluxes  
221 between our study and ON16 is not direct because they are during different hours of  
222 the simulation. However, the comparison period in this study (15-20 h) and ON16 (24-  
223 36 h) is generally during the same stage of the TC evolution, that is, a period just before  
224 and after the intensification rates become different, and therefore the comparison is  
225 reasonable. In addition, this study uses the total heat flux while ON16 just examine the  
226 latent heat flux. Detailed investigation of sensible and latent heat flux individually gives  
227 the same conclusion as the total heat flux.

228

#### 229 **4. Convection organization in directional shear flows**

230           Although balanced dynamics control the azimuthal position of convection  
231 during the early stage of development, they cannot explain all the features of convection  
232 organization in CW and CC hodographs at later times (hours 15 to 30), when  
233 differences in the magnitude and precession of the overall vortex tilts (Fig. 2) and the  
234 intensification rates (Fig. 1) begin to develop. Figures 5 and 6 show the time-averaged  
235 distribution of simulated radar reflectivity during hours 15–20, 20–25, and 25–30 for  
236 CW and CC hodographs, respectively. In CW hodographs during hours 15–20, the  
237 convection is located in the down-shear-left region in CW1.25 and CW2.5 (Figs. 5a  
238 and d) and near the left-of-shear region in CW5 (Fig. 5g). Between hours 20 and 25,  
239 the leading edge of the convective cluster in CW5 (Fig. 5h) advances into the up-shear-  
240 left region whereas the front edges of the convective clusters in CW1.25 and CW2.5  
241 (Figs. 5b and e) move into the left-of-shear region. After hour 25, all convection in CW  
242 hodographs has moved into the up-shear region (Figs. 5c, f and i). Therefore, although  
243 the tail of the convective cluster remains in the down-shear region, the leading edge of  
244 the convective cluster tends to organize near the left-of-shear and up-shear-left regions,  
245 and thus helps advance the overall vortex tilt into the up-shear region (Fig. 5). In  
246 contrast, in CC hodographs the leading edge of the convective cluster remains in the  
247 down-shear region but the convection tends to develop a tail structure extending from  
248 the main cluster in the down-shear region to the right-of-shear region (Figs. 3d-f and  
249 Fig. 6).

250           Furthermore, convection is organized quite differently in the radial direction  
251 between the two types of hodographs. In CW hodographs, the convection is confined  
252 within 120-km radius and is generally organized along the azimuth (Fig. 5). In CC

253 hodographs, in addition to the main convective cluster in the inner-region, there are  
254 indications of convection organization radially outward (150 km; Fig. 6). From hours  
255 15 to 20 (Fig. 6a), the main convective cluster in CC1.25 is located in the down-shear  
256 region. At the same time, weak signals of organized convection are established radially  
257 outward. After five hours (hours 20–25; Fig. 6b), the outer convection intensifies as the  
258 inner-core convection weakens slightly. The resulting distribution of convection  
259 exhibits a radially elongated pattern. Later, during hours 25–30, the inner convection  
260 weakens noticeably. As a result, the overall convection is located at larger radial  
261 distances (Fig. 6c). Similar organization also occurs in the CC2.5 and CC5. In CC2.5,  
262 the outer convection is initially organized in a spiral line along the azimuth during hours  
263 15–20 (Fig. 6d), and later (hours 20–25) intensifies as it merges with the weakening  
264 convection in the inner region, resulting in a rain-band along the radial direction (Fig.  
265 6e). Finally (hours 25–30), the overall convection weakens and shifts to cover a more  
266 radially outward region (Fig. 6f). In CC5 during hours 15–20, the outer convection has  
267 already merged with the inner-core convection, covering a large area in the down-shear-  
268 right quadrant (Fig. 6g). Later (hours 20–25), the outer convection maintains its strength  
269 and location as the inner convection weakens (Fig. 6h). Consequently, the remaining  
270 convection is concentrated in the outer region in the down-shear-right quadrant (Fig.  
271 6i).

272 To investigate the mechanism of convection organization, the vertical  
273 acceleration is decomposed into buoyancy and dynamic forcings (Jeevanjee and Romps  
274 2013). The relative roles of these two forcing could be quantified by diagnosing the  
275 vertical buoyancy acceleration  $a_b$  and the vertical inertial acceleration  $a_i$ . These two  
276 accelerations could be calculated by solving the Poisson equation for  $a_b$  and  $a_i$ ,

277

278 
$$-\nabla^2(\bar{\rho}a_b) = g\nabla_h^2\rho \quad ,$$

279 
$$-\nabla^2(\bar{\rho}a_i) = -\partial_z\nabla\cdot[\bar{\rho}(\mathbf{u}\cdot\nabla)\mathbf{u}] \quad ,$$

280 where  $\mathbf{u}$  is the three-dimensional wind vector,  $g$  is the gravitational acceleration,  $\rho$  is  
 281 air density and  $\bar{\rho}$  is the reference density.  $\nabla^2$  is the three-dimensional Laplacian,  $\nabla_h^2$   
 282 is the horizontal Laplacian, and  $\nabla\cdot$  is the three-dimensional divergence operator.  
 283 Figure 7 shows the total vertical acceleration (Figs. 7c and f), its dynamic component  
 284 (Figs. 7a and d), and its thermodynamic component (Figs. 7b and e) below 1.5 km  
 285 during hours 19–20 for CW2.5 (Figs. 7a–c) and CC2.5 (Figs. 7d–f). The dynamic  
 286 forcing outweighs the thermodynamic forcing in both CW2.5 and CC2.5. This is also  
 287 the case generally during hours 15–30 and in other simulations (including the sensitivity  
 288 experiments following the deactivation of diabatic heating and surface heat fluxes, not  
 289 shown) and therefore suggests that the surface heat flux may not play a direct role in  
 290 convection organization. In addition, the surface convergence does not coincide well  
 291 with the strong surface heat fluxes during hours 15–25 (not shown). Therefore, the  
 292 strong heat flux does not appear to feedback directly to assist the continuous  
 293 advancement of convection into the up-shear side. However, in CW hodographs, the  
 294 strong heat flux does begin to overlap with surface convergence once the overall vortex  
 295 tilt precesses into the up-shear side and favoring subsequent rapid intensification.

296 There are several possible dynamic mechanisms of convection organization in  
 297 directional shear flows. One involves kinematic structural changes in response to vortex  
 298 tilt, which has its roots in dry dynamics, as described by GTQ18, and is partly  
 299 responsible for differences in the azimuthal location of convection. Another is related  
 300 to storm movement. A northward component of TC movement exists in CW  
 301 hodographs, but a southward component exists in CC hodographs. This results in  
 302 different structures of asymmetric radial inflows (see Fig. 8 in GTQ18). Figure 8 shows

303 the distribution of radial flows within the boundary layer (0-1.5 km) over 15-25 h. In  
304 CW hodographs, the strongest inflow is located in the left-of-shear side. The radial inflows  
305 tend to occur in the up-shear-left quadrant in CW2.5 and CW5 simulations and lead the  
306 strong upward motions. This corresponds to the continuous organization of convection on  
307 the left-of-shear side in CW hodographs. In CC hodographs, a large part of the radial  
308 inflows come from the right-of-shear side. The stronger the southward environmental flow  
309 (CC5>CC2.5>CC1.25) is, the stronger the radial inflow on the right-of-shear side because  
310 the southward movement is stronger due to the enhanced vertically averaged steering flow.  
311 Therefore, the different asymmetric structures of boundary layer inflows may be  
312 responsible for the long tail in the right-of-shear region in CC hodographs, and favors  
313 further extension of the leading edge of convection into the left-of-shear region in CW  
314 hodographs. Finally, the mechanism proposed by Riemer (2016) may support  
315 convection organization in the radial direction outside the eyewall in CC hodographs.  
316 The overlap of asymmetric frictional convergence due to vortex tilt and low-level high-  
317 entropy air associated with the deformed moist envelope may favor deep convection in  
318 the down-shear-right region. Cold-pool dynamics are an alternative mechanism that  
319 may explain TC convection organization (e.g., Davis 2015). However, a detailed  
320 examination indicates that cold pools associated with convection are not in an optimal  
321 configuration with respect to local vertical wind shear along the azimuthal direction.  
322 The weakening of cyclonic circulation with height (not shown) due to the baroclinic  
323 nature of TCs leads to a horizontal vorticity that has the same sign as the baroclinically  
324 generated horizontal vorticity due to the cold pool. This does not support upright  
325 convection and thus is not favorable for convective organization azimuthally (Rotunno  
326 et al. 1988). The relative contributions of these possible mechanisms is not easy to  
327 distinguish because it is difficult to further decompose the dynamic forcing into

328 different components associated with these mechanism and thus will be left for a future  
329 study.

330 Differences in convection organization between CW and CC hodographs result  
331 in different mid-troposphere humidity and surface heat fluxes in the downwind region  
332 of overall vortex tilt. Figure 9 shows the time evolution of relative humidity in the mid-  
333 troposphere (4–8 km) for azimuth angles of  $30^\circ$  to  $60^\circ$  in the downstream region from  
334 the overall vortex tilt within an annular region 30–150 km from the TC center. Although  
335 the relative humidity in all the directional shear flows is similar for the first 15 hours,  
336 it increases continuously to 90% until hour 30 in CW hodographs, whereas in CC  
337 hodographs it begins to decrease from hours 15 to 20 with a drier downstream  
338 environment when the intensification occurs. This is because of differing convection  
339 organization in the azimuth due to TC movement and the relative configuration of the  
340 low-level vortex tilt with respect to the overall vortex tilt. An alternative explanation  
341 might be related with the mid-level advection. In the CW hodographs, the southerly  
342 environmental mean flow may advect the moist envelop to the downwind region of  
343 overall vortex tilt, resulting in a moist mid-troposphere. In the CC hodographs, the  
344 moist envelop is more easily advected to the right of overall vortex tilt due to the  
345 northerly environmental mean flow, leaving a drier mid-troposphere in the downwind  
346 region of overall vortex tilt. Surface heat flux also presents contrasting features in  
347 directional shear flows. Figure 10 shows that the surface heat flux in CW hodographs  
348 (Figs. 10a–c) is much stronger than that in CC hodographs (Figs. 10d–f) during hours  
349 25–30. This is because the convection at small radii is weaker because of the continuous  
350 organization of convection radially outward along with low-entropy downdrafts located  
351 in a region with lower wind speeds in CC hodographs.

352 Gu et al. (2015) showed that shear-induced convection outside the eyewall can  
353 transport moisture upward above the boundary layer, thus reducing the radial gradient  
354 of moist entropy and decreasing the output work of TC heat engine, and potentially  
355 weakening the TC during its mature stage. Figure 11 shows the time evolution of  
356 azimuthally averaged moist entropy in the inner (0–80 km) and outer (100–180 km)  
357 regions, and the difference between these two regions. The moist entropy difference  
358 between the inner and outer regions in CW hodographs is larger than that in CC  
359 hodographs throughout the simulated TC lifetime. During hours 20–30, the moist  
360 entropy in the inner region in CC1.25 and CC2.5 increases more rapidly ( $>5 \text{ J kg}^{-1} \text{ K}^{-1}$ )  
361  $^1$ ) than in CW cases ( $<5 \text{ J kg}^{-1} \text{ K}^{-1}$ ; Fig. 11a). However, the moist entropy in the outer  
362 region in CC1.25 and CC2.5 also increases ( $>5 \text{ J kg}^{-1} \text{ K}^{-1}$ ) more rapidly than in CW  
363 hodographs (nearly constant; Fig. 11b), and thus results in a weaker moist entropy  
364 difference between the inner and outer regions in CC1.25 and CC2.5 than in CW  
365 hodographs (Fig. 11c). Although the radial gradient of moist entropy increases in  
366 CC1.25 and CC2.5, rapid increases are inhibited by the continuous organization of  
367 convection at outer radii. In CC5, convection within the inner region is effectively  
368 weakened by a more intense organization of convection in the outer region (Figs. 6g–i)  
369 and also results in a weaker increase in the radial gradient of moist entropy than in CW  
370 hodographs (Figs. 11a and c). As a result, in CC hodographs the convection in the outer  
371 region prevents the radial gradient of moist entropy from increasing rapidly and thus  
372 may inhibit TC intensification. This is consistent with the importance of shear-induced  
373 outer convection in changing the radial gradient of moist entropy and thus TC intensity,  
374 although here we focus on the early stage rather than the mature stage of TC  
375 development.

376 Differences in convection organization lead to distinct dynamic structures, in  
377 addition to thermodynamic structures. Figure 12 shows the radial distribution of  
378 azimuthally averaged potential vorticity (PV) at heights of 2–5 km during hours 20–25.  
379 The TCs in CC hodographs have smaller PV in the inner region and larger PV in the  
380 outer region than in CW hodographs. This is because continuous organization of  
381 convection radially outward in CC hodographs redistributes the PV through convective  
382 heating and also generates PV through vortex stretching, resulting in a broader PV skirt  
383 with smaller negative radial gradients than in CW hodographs. Theoretical studies  
384 (Schechter et al. 2003; Reasor et al. 2004) have shown that TCs with larger magnitudes  
385 of the negative radial gradient of the PV skirt are more resilient in shear flows. This  
386 suggests that tilted TCs in CC hodographs are more likely to be further tilted away by  
387 shear flows, thus reducing the precession rate.

388

### 389 **5. Roles of convective heating in vortex precession**

390 As described in the last two sections, dry dynamics and other processes (e.g.,  
391 TC movement) set up distinct organizations of convection that result in quite different  
392 dynamic (PV skirt) and thermodynamic (downwind mid-troposphere relative humidity,  
393 surface heat flux and radial gradient of moist entropy within inner-core region)  
394 structures in directional shear flows. A critical issue is how these structural differences  
395 couple to affect the overall vortex tilt and TC intensification rates.

396 An important component of moist convection is latent heat release, whose role  
397 can be investigated by directly comparing moist simulations with the dry simulations  
398 of GTQ18, as they used the same experimental and model setups except for the  
399 inclusion of moist convection. Figure 13 shows the time evolution of overall vortex tilt  
400 in terms of magnitude and direction for both moist and dry simulations. Convective

401 heating has two effects on the evolution of vortex tilt. The first is that convective heating  
402 aids the coupling between vortices at different levels, and thus prevents further  
403 departures of upper-level vortices from low-level vortices. Moist convection begins to  
404 take effect before hour 10 and tends to reduce the vortex tilt in both CW and CC  
405 hodographs (Figs. 13a and b). Although the magnitude of the vortex tilt decreases after  
406 the vortex tilt precesses into the up-shear region, the timing of its decrease is generally  
407 ahead of the timing of the up-shear precession in CW hodographs (Figs. 13a and c).  
408 This indicates that convective heating first aids the coupling between low-level and  
409 upper-level circulation and prevents the amplitude of overall vortex tilt from increasing  
410 rapidly.

411         The second effect is that enhanced coupling also leads to higher precession rates  
412 during the early stage (hours 0–15). The overall vortex tilt in all CC hodographs and  
413 CW1.25 precesses faster than in the corresponding dry simulations from hour 5 to hour  
414 15 (Figs. 13c and d). The precession rates in CW2.5 and CW5 are generally the same  
415 as the dry simulations during this period. After hour 15, the precession rates of overall  
416 vortex tilt further accelerate in CW hodographs (Fig. 13c). To explore whether  
417 convective heating favors precession, we perform sensitivity simulations by reducing  
418 the convective heating from hours 15 to 25 in the CW2.5 simulation (see details in  
419 section 2). We choose CW2.5 to conduct sensitivity experiments because the overall  
420 vortex tilt in this simulation has a moderate precession rate (compared to CW1.25 and  
421 CW5) and ends up oriented up-shear. Sensitivity simulations based on CW1.25 and  
422 CW5 lead to similar results. After convective heating is suppressed, the precession rate  
423 remains the same as in CW2.5 from hours 15 to 20 and then begins to decrease after  
424 hour 20 (Fig. 14a). The overall vortex tilt reaches the left-of-shear region ( $90^\circ$ ) around  
425 hour 35, about 10 hours later than in CW2.5 (Fig. 14a). The leading edge of the

426 convective cluster also retrogresses after latent heating is weakened (not shown). As a  
427 result, the magnitude of the vortex tilt increases and its decrease begins later (Fig. 14b).  
428 The TC intensity also weakens in response to the delayed precession and increased  
429 vortex tilt magnitude after reducing the diabatic heating. These sensitivity simulations  
430 suggest a favorable role for convective heating in supporting the continuous precession  
431 of vortex tilt in CW hodographs. Another interesting feature is that the overall vortex  
432 tilt still precesses into the up-shear region in CW2.5\_0DH, in which all the convective  
433 heating has been turned off during hours 15–20. This strongly indicates that dry  
434 dynamics still have an effect in moist simulations. However, convective heating does  
435 not always favor the precession of vortex tilt. After hour 15, the precession rates in CC  
436 hodographs decrease to zero (CC1.25) or even become negative (CC2.5 and CC5),  
437 indicating that the tilted vortex stops precessing cyclonically and is pulled back toward  
438 the down-shear-right region (Fig. 13d). This happens during the period when the  
439 convection becomes organized both in the radially outer region and in the azimuthally  
440 right-of-shear region (Fig. 6). Continuous organization of convection in CC hodographs  
441 results in stronger convective heating in the outer region. Figure 15 shows results from  
442 an isentropic analysis (e.g., Paulius and Mrowiec 2013) of diabatic heating in the outer  
443 region (100–200 km) during hours 15–30. Isentropic analysis facilitates a separation of  
444 air parcels between warm, moist updrafts and cold, dry downdrafts that are fundamental  
445 aspects of moist convection and has been applied in recent studies of TCs (e.g.,  
446 Mrowiec et al. 2016; Fang et al. 2017). It provides a cleaner way to compare the  
447 magnitudes of diabatic heating in ascending air streams between the simulations with  
448 different hodographs. The magnitudes of diabatic heating in CC hodographs are almost  
449 two times those in CW hodographs, particularly above 5 km (Figs. 15c–e). Strong  
450 convective heating in the outer region induces secondary circulations that weaken the

451 radial inflow toward the TC center and suppress vertical motion in the inner region.  
452 Therefore, the persistence of convection in the outer region from the right-of-shear  
453 region to the down-shear region has a negative impact on inner-core convection and  
454 explains the weakening of convection with time at smaller radii in CC hodographs (Fig.  
455 6). In addition, strong convective heating above the mid-level generates cyclonic  
456 vorticity radially outward, thus increasing the magnitude of the overall vortex tilt and  
457 inhibiting tilt precession (Figs. 13b and d).

458 In addition to the effects of convective heating, it is reasonable to hypothesize  
459 that differences in the distribution of surface heat flux also contribute to differences in  
460 precession rates, as the surface heat flux in CW hodographs is stronger and closer to  
461 the up-shear region than in CC hodographs (Fig. 10). Although the position and strength  
462 of strong surface heat fluxes are controlled primarily by the distribution of convection  
463 (see section 3), the feedback from surface heat fluxes may contribute to the continuous  
464 advancement of convective clusters in CW hodographs, as air parcels with large surface  
465 heat fluxes can be ingested into the TC core more frequently (ON16). However, it is  
466 unclear whether convective heating or the feedback from strong surface heat fluxes is  
467 more important for the continuous precession of overall vortex tilt. To investigate this,  
468 sensitivity simulations CW2.5\_0.5MSF and CW2.5\_0MSF are performed by removing  
469 the strong surface heat flux in the downstream region of the convective cluster during  
470 hours 15–25, based on the CW2.5 simulation (see section 2). Results show that the  
471 evolution of vortex tilt in the sensitivity simulations, in terms of both precession rate  
472 and magnitude, generally remain the same as in the control simulation (CW2.5)  
473 throughout the integration except in CW2.5\_0SF, in which all the surface heat flux is  
474 turned off (Fig. 16). Furthermore, the leading edge of convective clusters in the  
475 sensitivity experiments stays close to that in CW2.5 and the TC intensity changes little

476 during this period though it weakens later (not shown). This suggests that it is the  
477 convective heating, rather than the strong surface heat flux in the downstream region of  
478 the convective cluster, that plays a leading role of controlling the precession rate of  
479 overall vortex tilt. Strong surface heat fluxes may provide favorable environments for  
480 convection organization in up-shear regions but do not directly affect the precession of  
481 overall vortex tilt. These fluxes will provide energy for convection and affect the  
482 precession through diabatic heating at later stages.

483

## 484 **6. Discussion**

485 Vortex tilt precession and up-shear propagation of convection are key processes  
486 by which TCs intensify in vertical wind shear and have been the focus of recent studies.  
487 Munsell et al. (2017) emphasized the role of vortex precession in aiding the up-shear  
488 propagation of convection in their ensemble simulation of Hurricane Edouard (2014).  
489 Observational studies (Rogers et al. 2016; Zawislak et al. 2016) of Hurricane Edouard  
490 focused on environments, such as mid-level relative humidity in the up-shear region  
491 and sea-surface temperatures in the right-of-shear region, that support the persistence  
492 of deep convection in the up-shear region and thus contribute to vortex tilt precession  
493 and TC intensification. Using idealized simulations, ON14 and ON16 emphasized the  
494 importance of various structures, including the distributions of helicity and convection  
495 and associated surface heat flux relative to the shear vector, in assisting the up-shear  
496 advancement of convection in directional shear flows. Therefore, it is unclear if the  
497 propagation of convection into the up-shear region is a result or a cause of the overall  
498 vortex tilt precession.

499 Here, we propose that these two processes closely interact with each other in  
500 directional shear flows, both constructively and destructively, depending on convection

501 organization. This study investigates the dynamics that result in distinct TC structural  
502 features and how these structures couple with the overall vortex tilt through feedbacks  
503 from convective heating in directional shear flows. The position and organization of  
504 convective clusters in directional shear flows are first determined as a balanced  
505 response to the vortex tilt and are then influenced by TC movement and other dynamics.  
506 Convective heating plays an important role in coupling of vortices at different levels  
507 and also affects vortex tilt precession. Whether convective heating favors the  
508 continuous precession of vortex tilt depends on the organization of convection, which  
509 is controlled by both dry and moist dynamics. In CW hodographs, favorable convection  
510 organization enhances the feedback from convective heating and induces the overall  
511 vortex tilt to advance into a region with strong surface heat flux and a humid mid-  
512 troposphere, favoring further organization and a strengthening of convection, thus  
513 forming a positive feedback. In CC hodographs, unfavorable organization in the  
514 azimuthally upwind region and in the radially outward region of convective clusters  
515 makes the precession of vortex tilt more difficult. This organization acts to vertically  
516 decouple the vortex and thus slows the precession of overall vortex tilt. In addition, the  
517 thermodynamic environment (a weak surface heat flux and dry mid-troposphere) in the  
518 downstream region of the overall vortex tilt is less conducive to persistent deep  
519 convection. As a result, a negative feedback is established and hinders the precession  
520 of vortex tilt and the advancement of convective clusters in CC hodographs.

521 A recent observational study (Chen et al. 2018) found that the relative  
522 configuration of low-level mean flow (LMF, i.e. 850 hPa mean flow) and deep-layer  
523 vertical wind shear is important in determining TC structure and intensity change. The  
524 LMF directed to the left (right) of the deep-layer shear is called left-of-shear (right-of-shear)  
525 LMF, corresponding to the LMF in CW (CC) hodographs. A left-of-shear LMF favors

526 TC intensification whereas a right-of-shear orientation of LMF favors an increase in  
527 TC size. This is consistent with our findings for directional shear flows. In CW  
528 hodographs, TC-relative LMF is directed toward a left-of-shear orientation and  
529 supports the continuous precession of convective clusters into the up-shear region,  
530 leading to TC intensification. In CC hodographs, TC-relative LMF is orientated toward  
531 the right-of-shear region, favoring convection organization in the outer region to  
532 broaden the PV skirt and thus leads to increases in size rather than intensification.

533

## 534 **7. Summary**

535 This study investigated the coupling between vortex tilt and convection  
536 organization, and its impact on TC intensification in directional shear flows. A  
537 comparison with dry simulations revealed the importance of the feedback from moist  
538 convection through convective heating, although dry dynamics can explain a large part  
539 of the TC structural differences between CW and CC hodographs.

540 During the early stage of development, the overall vortex tilt is generally  
541 directed toward the down-shear-left region in CW hodographs and the down-shear-right  
542 region in CC hodographs. This is consistent with the balanced response to the height-  
543 dependent vortex tilt and explains subsequent differences in the azimuthal distribution  
544 of moist convection. Once the positions of convective clusters are determined, strong  
545 surface heat fluxes occur in the downstream region, primarily because of the  
546 thermodynamic disequilibrium reservoir established by low-entropy downdrafts  
547 associated with precipitation. Therefore, large variability in TC structures in directional  
548 shear flows during the early stage is well explained by vortex tilt-dominated dry  
549 dynamics, even in moist simulations.

550 Convective heating favors coupling between vortex centers at different levels,  
551 and thus reduces the vortex tilt magnitude compared with dry simulations and then  
552 accelerates precession in both CW and CC hodographs during the early stage.  
553 Afterwards in CW hodographs, the precession of vortex tilt, together with TC  
554 movement, favors organization of convection in the downstream region of overall  
555 vortex tilt because of the strong surface heat flux and moist mid-troposphere. A positive  
556 feedback among vortex tilt, organized convection, and convective heating is established.  
557 As a result, the precession of vortex tilt is further accelerated and reaches the up-shear-  
558 left region, which aids the reduction in vortex tilt and subsequently leads to  
559 intensification. However, in CC hodographs, the convective heating associated with the  
560 continuous organization of convection in outer regions and azimuthally upwind regions  
561 tends to vertically decouple the vortex and weakens their coupling. Given that the  
562 downstream region has both a weak surface heat flux and a dry mid-troposphere, a  
563 negative feedback is established that concentrates convective heating mainly in the  
564 down-shear-right and radially outward region. Consequently, the cyclonic precession  
565 of vortex tilt through the down-shear-left region gradually slows, or even retrogresses  
566 to the down-shear-right region. This results in a continuous increase in overall vortex  
567 tilt magnitude by deep-layer shear and thus prevents TC intensification in CC  
568 hodographs.

569

570 *Acknowledgement* We thank Dr. David S. Nolan and Dr. Matthew J. Onderlinde for  
571 their suggestions on the implementation of PDS method in the WRF model, and Dr.  
572 Nadir Jeevanjee for providing the code to decompose the vertical acceleration into  
573 thermodynamic and dynamical components. The first author also thanks Dr.  
574 Christopher E. Holloway for helpful discussion. The authors also thank two anonymous

575 reviewers for their critical comments that improve our manuscript. This work is jointly  
576 supported by the National Key R&D Program of China under Grants 2017YFC1501601,  
577 the National Natural Science Foundation of China (41505044, 41575053, 41675053),  
578 National Key Project for Basic Research (973 Project) under Grant 2015CB452803.

579 **Reference**

580 Chen, B.-F., C. A. Davis and Y.-H. Kuo, 2018: Effects of low-level flow orientation  
581 and vertical wind shear on the structure and intensity of tropical cyclones. *Mon.*  
582 *Wea. Rev.*, **146**, 2447-2467.

583 Chen, X., Y. Wang, J. Fang and M. Xue, 2018: A numerical study on rapid  
584 intensification of Typhoon Vicente (2012) in the South China Sea. Part II: Roles  
585 of inner-core processes. *J. Atmos. Sci.*, **75**, 235-255.

586 Davis, A. C., 2015: The formation of moist vortices and tropical cyclones in idealized  
587 simulations. *J. Atmos. Sci.*, **72**, 3499-3516.

588 Fang, J., O. M. Paulius, and Fuqing Zhang, 2017: Isentropic analysis on the  
589 intensification of Hurricane Edouard (2014). *J. Atmos. Sci.*, **74**, 4177-4197.

590 Frank, W. M., and E. A. Ritchie, 1999: Effects of environmental flow upon tropical  
591 cyclone structure. *Mon. Wea. Rev.*, **127**, 2044–2061.

592 Gu, J.-F., Z.-M. Tan, and X. Qiu, 2015: Effects of vertical wind shear on inner-core  
593 thermodynamics of an idealized simulated tropical cyclone. *J. Atmos. Sci.*, **72**,  
594 511–530.

595 —, —, and —, 2016: Quadrant-dependent evolution of low-level tangential  
596 wind of a tropical cyclone in the shear flow. *J. Atmos. Sci.*, **73**, 1159-1177.

597 —, —, and —, 2018: The evolution of vortex tilt and upward motion of tropical  
598 cyclones in directional shear flows. *J. Atmos. Sci.*, **75**, 3565-3578.

599 Hide, R., 2002: Helicity, superhelicity and weighted relative potential vorticity:  
600 Useful diagnostic pseudoscalars? *Q. J. R. Meteorol. Soc.*, **128**, 1759-1762.

601 Hong, S-Y., and J-O. J. Lim, 2006: The WRF single-moment 6-class microphysics  
602 scheme (WSM6). *J. Korean Meteor. Soc.*, **42**, 129-151.

603 ———, and Y. Noh, and J. Dudhia, 2006: A new vertical diffusion package with an  
604 explicit treatment of entrainment processes. *Mon. Wea. Rev.*, **134**, 2318–2341.

605 Jeevanjee, N., and D. M. Romps, 2015: Effective buoyancy, inertial pressure, and the  
606 mechanical generation of boundary layer mass flux by cold pools. *J. Atmos. Sci.*,  
607 **72**, 3199-3213.

608 Mrowiec, A. A., O. M. Paulius, and F. Zhang, 2016: Isentropic analysis of a simulated  
609 hurricane. *J. Atmos. Sci.*, **73**, 1857-1870.

610 Munsell, E. B., F. Zhang, J. A. Sippel, S. A. Braun and Y. Weng, 2017: Dynamics and  
611 predictability of the intensification of Hurricane Edouard (2014). *J. Atmos. Sci.*,  
612 **74**, 573-593.

613 Nolan, D. S., 2011: Evaluating environmental favorableness for tropical cyclone  
614 development with the method of point-downscaling. *J. Adv. Model. Earth Syst.*, **3**,  
615 1-28.

616 Onderlinde, M. J., and D. S. Nolan, 2014: Environmental helicity and its effects on  
617 development and intensification of tropical cyclones. *J. Atmos. Sci.* **71**, 4308-  
618 4320.

619 ———, and ———, 2016: Tropical cyclone-relative environmental helicity and the  
620 pathways to intensification in shear. *J. Atmos. Sci.*, **73**, 869-890.

621 Pauluis, O. M., and A. A. Mrowiec, 2013: Isentropic analysis of convective motions. *J.*  
622 *Atmos. Sci.*, **70**, 3673–3688.

623 Rappin, E. D., and D. S. Nolan, 2012: The effects of vertical shear orientation on  
624 tropical cyclogenesis. *Quart. J. Roy. Meteor. Soc.*, **138**, 1035-1054.

625 Reasor, P. D., M. T. Montgomery, and L. D. Grasso, 2004: A new look at the problem  
626 of tropical cyclones in vertical wind shear flow: Vortex resiliency. *J. Atmos. Sci.*,  
627 **61**, 3-22.

628 Riemer, M., 2016: Meso- $\beta$ -scale environment for the stationary band complex of  
629 vertically sheared tropical cyclones. *Quart. J. Roy. Meteor. Soc.*, **142**, 2442–  
630 2451.

631 Rogers, R. F., Jun A. Zhang, J. Zawislak, H. Jiang, G. R. Alvey, E. J. Zipser, S. N.  
632 Stevenson, 2016: Observations of the structure and evolution of Hurricane  
633 Edouard (2014) during intensity change. Part II: Kinematic structure and the  
634 distribution of deep convection. *Mon. Wea. Rev.*, **144**, 3355-3376.

635 Rotunno, R., J. B. Klemp, and M. L. Weisman, 1988: A theory for strong, long-lived  
636 squall lines. *J. Atmos. Sci.*, **45**, 463–485.

637 Schechter, D. A., and M. T. Montgomery and P. D. Reasor, 2002: A theory for the  
638 vertical alignment of a quasi-geostrophic vortex. *J. Atmos. Sci.*, **59**, 150-168.

639 Skamarock, W. C., J. B. Klemp, J. Dudhia, D. O. Gill, D. M. Barker, M. G. Duda, X.-  
640 Y. Huang, W. Wang, and J. G. Powers, 2008: A description of the advanced  
641 research WRF version 3. *NCAR technical note 475+STR*, 113pp.

642 Stevenson, S. N., K. L. Corbosiero, and J. Molinari, 2014: The convective evolution  
643 and rapid intensification of Hurricane Earl (2010). *Mon. Wea. Rev.*, **142**, 4344-  
644 4380.

645 Tan, Z.-M. and R. Wu, 1994: Helicity dynamics of atmospheric flow. *Adv. Atmos. Sci.*,  
646 **11**, 175-188.

647 Wang, Y., Y. Rao, Z.-M. Tan, and D. Schönemann, 2015: A statistical analysis of the  
648 effects of vertical wind shear effects on tropical cyclone intensity change over  
649 the western North Pacific. *Mon. Wea. Rev.*, **143**, 3434-3453.

650 Zawislak, J., H. Jiang, G. R. Alvey III and E. J. Zipser, 2016: Observations of the  
651 structure and evolution of Hurricane Edouard (2014) during intensity change.  
652 Part I: Relationship between the thermodynamic structure and precipitation.  
653 *Mon. Wea. Rev.*, **144**, 3333-3354.

654

655 **List of Figures**

656

657 **FIG. 1.** (a) Hodographs of environmental flow in clockwise (CW) and counter-  
658 clockwise (CC) simulations. The environmental flow begins to rotate at 850 hPa and  
659 ceases at 200 hPa. The meridional component of environmental flow achieves its  
660 maximum magnitude at ~500 hPa in directional shear flows. The black solid line  
661 represents unidirectional shear flow. (b) Time evolution of TC intensity in terms of  
662 minimum sea-level pressure (hPa). Line colors in (a) and (b) indicate the simulation:  
663 CC5 (red), CC2.5 (brown), CC1.25 (yellow), CW1.25 (light blue), CW2.5 (blue), CW5  
664 (dark blue), and UNDIR (thick black).

665

666 **FIG. 2.** Time evolution of overall vortex tilt (0–8 km) magnitude (km; a) and tilt angle  
667 (degrees; b). The vortex center at each level is calculated as the vorticity centroid within  
668 a radius of 200 km from the location of minimum pressure. The tilt angle is calculated  
669 counterclockwise from east (i.e., 0° for east, 90° for north, 180° for west, 270° for  
670 south). Deep-layer vertical wind shear is directed to the east. Line colors indicate the  
671 simulation: CC5 (red), CC2.5 (brown), CC1.25 (yellow), CW1.25 (light blue), CW2.5  
672 (blue), CW5 (dark blue), and UNDIR (thick black).

673

674 **FIG. 3.** Plane view of maximum reflectivity (dBz, shaded) and local helicity ( $\text{m s}^{-2}$ ;  
675 black contours: 50, 200, 350) at hour 15: (a) CW1.25, (b) CW2.5, (c) CW5, (d) CC1.25,  
676 (e) CC2.5, and (f) CC5. The black shaded circle, magenta triangle, and black hollow  
677 circle represent the vortex centers at 2, 5, and 8 km height, respectively. Black contours  
678 represent the local helicity. The contour of  $200 \text{ m s}^{-2}$  is highlighted with thick black lines.

679 The thick black arrow at the bottom of the figure indicates the direction of deep-layer  
680 shear.

681

682 **FIG. 4.** Plane view of time-averaged (hours 15–20) surface heat flux (sum of latent heat  
683 flux and sensible heat flux; shading;  $\text{W m}^{-2}$ ) and equivalent potential temperature (black  
684 contours; K) at the surface for: (a) CW1.25, (b) CW2.5, (c) CW5, (d) CC1.25, (e) CC2.5,  
685 and (f) CC5. The white circle and square represent the vortex centers at 2 and 8 km  
686 height at hour 20, respectively. The thick black arrow at the bottom of the figure  
687 indicates the direction of deep-layer shear.

688

689 **FIG. 5.** Plane view of time-averaged reflectivity (dBz) in the innermost domain in  
690 simulations with CW hodographs: CW1.25 (first row; a–c), CW2.5 (second row; d–f),  
691 and CW5 (third row; g–i). The averaging period is hours 15–20 (first column; a, d, and  
692 g), 20–25 (second column; b, e, and h), and 25–30 (third column; c, f, and i). The thick  
693 black arrow at the bottom of the figure indicates the direction of deep-layer shear.

694

695 **FIG. 6.** Plane view of time-averaged reflectivity (dBz) in the innermost domain in  
696 simulations with CC hodographs: CC1.25 (first row; a–c), CC2.5 (second row; d–f),  
697 and CC5 (third row; g–i). The averaging period is hours 15–20 (first column; a, d, and  
698 g), 20–25 (second column; b, e, and h), and 25–30 h (third column; c, f, and i). The  
699 thick black arrow at the bottom of the figure indicates the direction of deep-layer shear.

700

701 **FIG. 7.** Plane view of the decomposition of vertical acceleration in simulations CW2.5  
702 (a–c) and CC2.5 (d–f) during hours 19–20: (a and d) inertial vertical acceleration ( $\text{m s}^{-2}$ );  
703 (b and e) effective buoyancy acceleration ( $\text{m s}^{-2}$ ); and (c and f) total vertical

704 acceleration ( $\text{m s}^{-2}$ ). Black contours (from  $1 \text{ m s}^{-1}$  to  $4 \text{ m s}^{-1}$  with  $1 \text{ m s}^{-1}$  interval)  
705 indicate vertical motion. The domain is chosen to ensure that the convection is near the  
706 center of the plot.

707

708 **FIG. 8.** Plane view of time averaged (15-25 h) radial velocity (shading;  $\text{m s}^{-1}$ ) within  
709 the boundary layer (0-1.5 km) and time averaged (15-25 h) positive vertical velocity  
710 (contours;  $\text{m s}^{-1}$ , every  $0.5 \text{ m s}^{-1}$  starting from  $0.5 \text{ m s}^{-1}$ ): (a) CW1.25, (b) CW2.5, (c)  
711 CW5, (d) CC1.25, (e) CC2.5, and (f) CC5. The thick black arrow at the bottom of the  
712 figure indicates the direction of deep-layer shear.

713

714 **FIG. 9.** Time evolution of relative humidity averaged over the mid-troposphere (4–8  
715 km) for azimuth angles of  $30^\circ$  to  $60^\circ$  in the downstream region of overall vortex tilt and  
716 within a radius of 30 to 150 km from the vortex center at a 2-km height in simulations  
717 of directional shear flows. Line colors indicate the simulation: CC5 (red), CC2.5  
718 (brown), CC1.25 (yellow), CW1.25 (light blue), CW2.5 (blue), and CW5 (dark blue).

719

720 **FIG. 10.** As for Fig. 4, but for time-averaged surface heat flux (sum of latent heat flux  
721 and sensible heat flux;  $\text{W m}^{-2}$ ) during hours 25–30. The white circle and square  
722 represent the vortex centers at heights of 2 and 8 km at hour 30, respectively.

723

724 **FIG. 11.** Time evolution of azimuthally averaged moist entropy and moist entropy  
725 difference between the inner- and outer-core regions over 4-8 km height: (a) moist  
726 entropy in the inner region (0–80 km); (b) moist entropy in the outer region (100–180  
727 km); (c) moist entropy difference between the inner and outer regions. Line colors

728 indicate the simulation: CC5 (red), CC2.5 (brown), CC1.25 (yellow), CW1.25 (light  
729 blue), CW2.5 (blue), and CW5 (dark blue).

730  
731 **FIG. 12.** Radial profile of azimuthally, vertically (2–5 km), and time-averaged (20–25  
732 h) potential vorticity (PV). Line colors indicate the simulation: CC5 (red), CC2.5  
733 (orange), CC1.25 (yellow), CW1.25 (light blue), CW2.5 (blue), and CW5 (dark blue).

734  
735 **FIG. 13.** Time evolution of overall vortex tilt (0–8 km) magnitude (km; a and b) and  
736 tilt direction (degrees; c and d) for moist (solid line) and dry (dash–dotted line)  
737 simulations: (a) tilt magnitude in CW hodographs; (b) tilt magnitude in CC hodographs;  
738 (c) tilt direction in CW hodographs; and (d) tilt direction in CC hodographs. The tilt  
739 angle is calculated counterclockwise from east (i.e., 0° for east, 90° for north, 180° for  
740 west, and 270° for south). The suffix ‘\_D’ denotes results from dry simulations and  
741 ‘\_M’ denotes results from the corresponding moist simulations.

742  
743 **FIG. 14.** Time evolution of overall vortex tilt (0–8 km) direction (degrees; a) and  
744 magnitude (km; b) for CW2.5 (blue solid) and the latent heating sensitivity simulations  
745 of CW2.5; i.e., CW2.5\_0.5DH (blue dashed) and CW2.5\_0DH (blue dashed–dotted).  
746 The two black vertical dashed lines denote the timings at which the deactivation of  
747 diabatic heating begins (15 h) and ends (25 h).

748  
749 **FIG. 15.** Isentropic distribution of time-averaged (hours 15–30) diabatic heating ( $\text{K s}^{-1}$ )  
750 <sup>1</sup>) within 100–200 km of the vortex center at 2-km height: (a) CW1.25, (b) CW2.5, (c)  
751 CW5, (d) CC1.25, (e) CC2.5, and (f) CC5. The abscissa is the equivalent potential  
752 temperature (EPT). The black solid line represents the domain-averaged vertical profile  
753 of equivalent potential temperature.

754

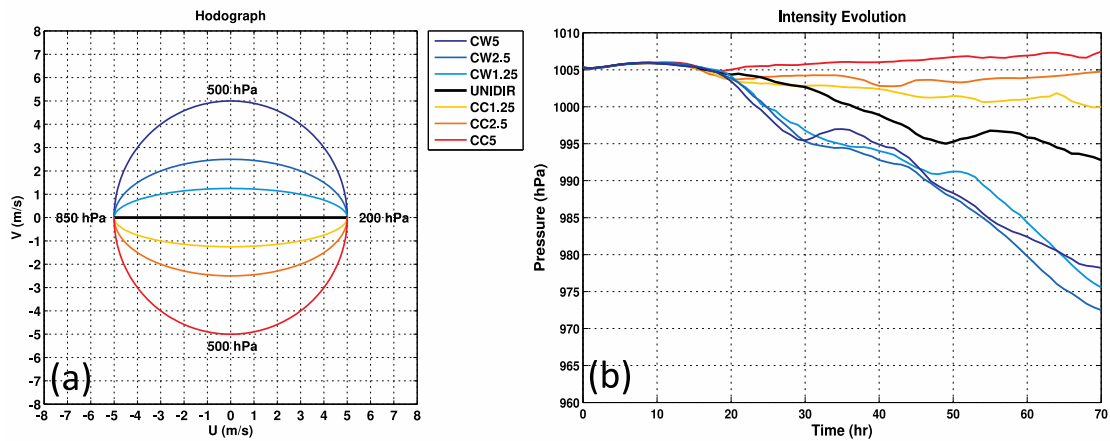
755 **FIG. 16.** Time evolution of overall vortex tilt (0–8 km) direction (degrees; a) and  
756 magnitude (km; b) for CW2.5 (blue solid) and the surface heat flux sensitivity  
757 simulations of CW2.5; i.e., CW2.5\_0.5MSF (blue dash) and CW2.5\_0MSF (blue  
758 dashed–dotted). The two black vertical dashed lines denote the timings at which the  
759 deactivation of diabatic heating begins (15 h) and ends (25 h).

760

761

762

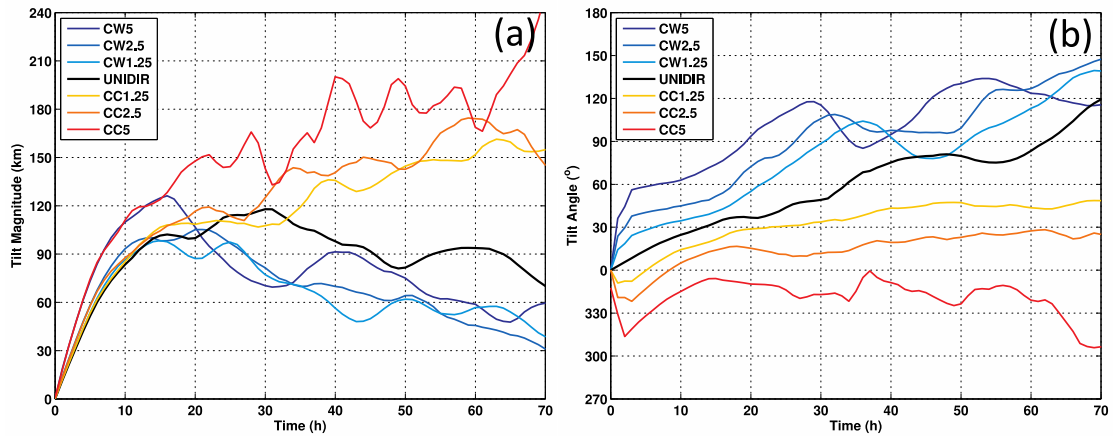
763



764

765 **FIG. 1.** (a) Hodographs of environmental flow in clockwise (CW) and counter-  
766 clockwise (CC) simulations. The environmental flow begins to rotate at 850 hPa and  
767 ceases at 200 hPa. The meridional component of environmental flow achieves its  
768 maximum magnitude at ~500 hPa in directional shear flows. The black solid line  
769 represents unidirectional shear flow. (b) Time evolution of TC intensity in terms of  
770 minimum sea-level pressure (hPa). Line colors in (a) and (b) indicate the simulation:  
771 CC5 (red), CC2.5 (brown), CC1.25 (yellow), CW1.25 (light blue), CW2.5 (blue), CW5  
772 (dark blue), and UNDIR (thick black).

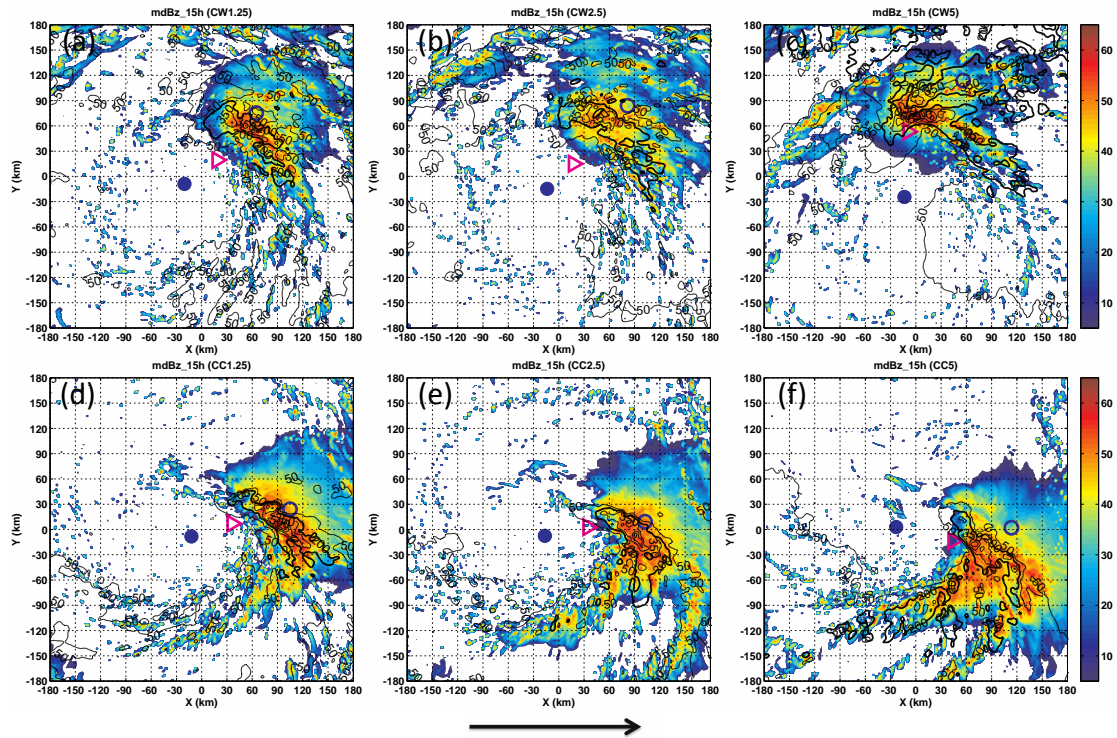
773



774

775 **FIG. 2.** Time evolution of overall vortex tilt (0–8 km) magnitude (km; a) and tilt angle  
 776 (degrees; b). The vortex center at each level is calculated as the vorticity centroid within  
 777 a radius of 200 km from the location of minimum pressure. The tilt angle is calculated  
 778 counterclockwise from east (i.e., 0° for east, 90° for north, 180° for west, 270° for  
 779 south). Deep-layer vertical wind shear is directed to the east. Line colors indicate the  
 780 simulation: CC5 (red), CC2.5 (brown), CC1.25 (yellow), CW1.25 (light blue), CW2.5  
 781 (blue), CW5 (dark blue), and UNDIR (thick black).

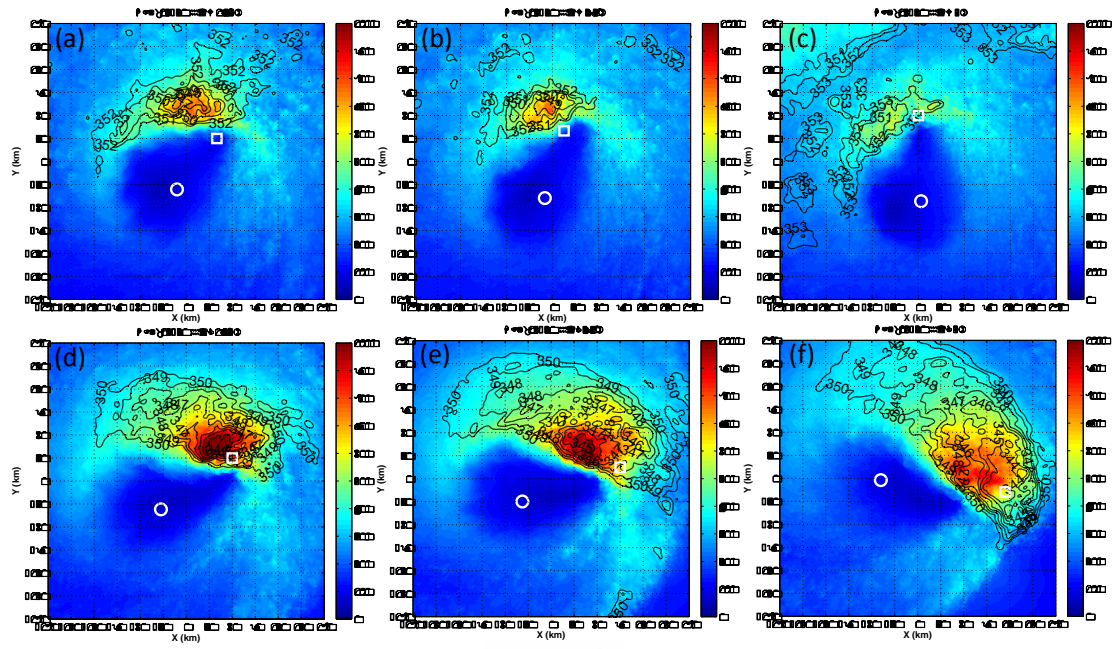
782



783

784 **FIG. 3.** Plane view of maximum reflectivity (dBz, shaded) and local helicity ( $\text{m s}^{-2}$ ;  
 785 black contours: 50, 200, 350) at hour 15: (a) CW1.25, (b) CW2.5, (c) CW5, (d) CC1.25,  
 786 (e) CC2.5, and (f) CC5. The black shaded circle, magenta triangle, and black hollow  
 787 circle represent the vortex centers at 2, 5, and 8 km height, respectively. Black contours  
 788 represent the local helicity. The contour of  $200 \text{ m s}^{-2}$  is highlighted with thick black lines.  
 789 The thick black arrow at the bottom of the figure indicates the direction of deep-layer  
 790 shear.

791



792

793

794

795

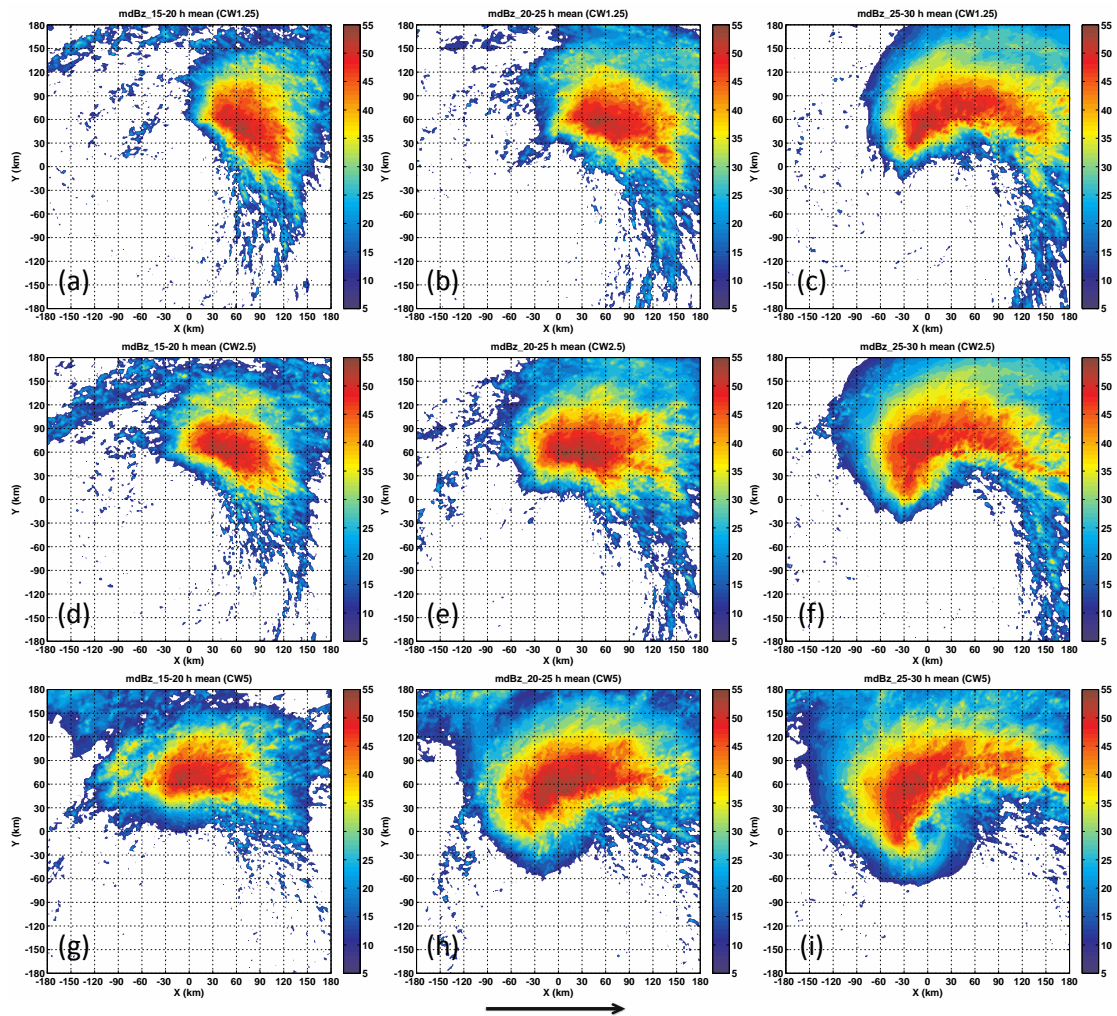
796

797

798

799

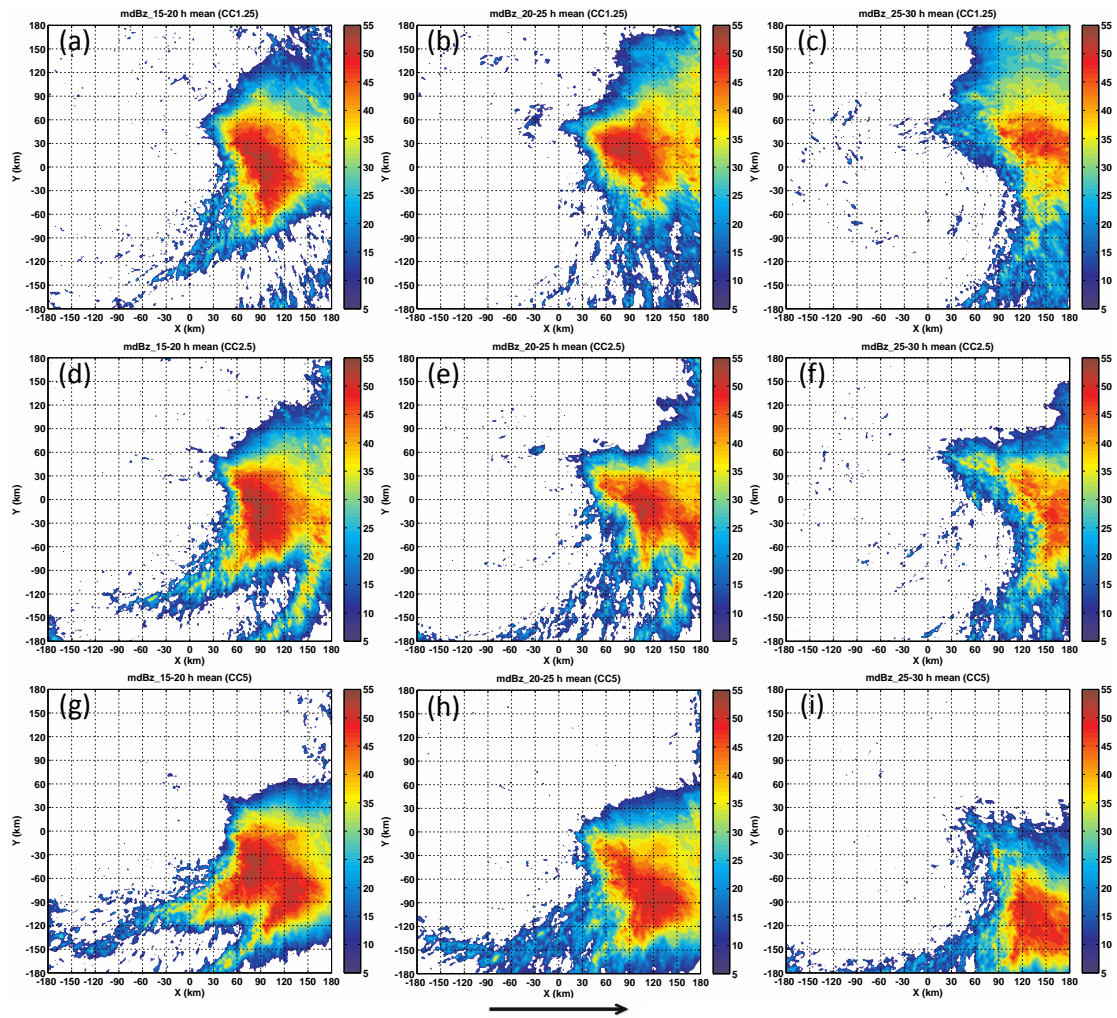
**FIG. 4.** Plane view of time-averaged (hours 15–20) surface heat flux (sum of latent heat flux and sensible heat flux; shading;  $\text{W m}^{-2}$ ) and equivalent potential temperature (black contours; K) at the surface for: (a) CW1.25, (b) CW2.5, (c) CW5, (d) CC1.25, (e) CC2.5, and (f) CC5. The white circle and square represent the vortex centers at 2 and 8 km height at hour 20, respectively. The thick black arrow at the bottom of the figure indicates the direction of deep-layer shear.



801

802 **FIG. 5.** Plane view of time-averaged reflectivity (dBz) in the innermost domain in  
 803 simulations with CW hodographs: CW1.25 (first row; a–c), CW2.5 (second row; d–f),  
 804 and CW5 (third row; g–i). The averaging period is hours 15–20 (first column; a, d, and  
 805 g), 20–25 (second column; b, e, and h), and 25–30 (third column; c, f, and i). The thick  
 806 black arrow at the bottom of the figure indicates the direction of deep-layer shear.

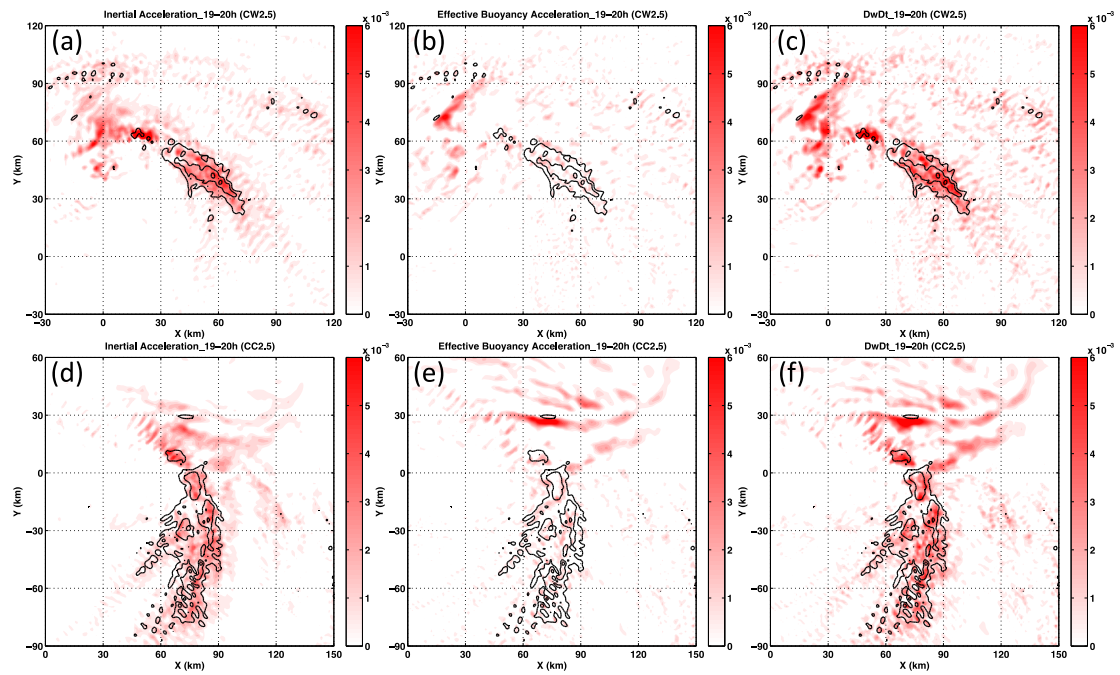
807



808

809 **FIG. 6.** Plane view of time-averaged reflectivity (dBZ) in the innermost domain in  
 810 simulations with CC hodographs: CC1.25 (first row; a–c), CC2.5 (second row; d–f),  
 811 and CC5 (third row; g–i). The averaging period is hours 15–20 (first column; a, d, and  
 812 g), 20–25 (second column; b, e, and h), and 25–30 h (third column; c, f, and i). The  
 813 thick black arrow at the bottom of the figure indicates the direction of deep-layer shear.

814



815

816

817 **FIG. 7.** Plane view of the decomposition of vertical acceleration near surface (0-0.5

818 km) in simulations CW2.5 (a-c) and CC2.5 (d-f) during hours 19–20: (a and d) inertial

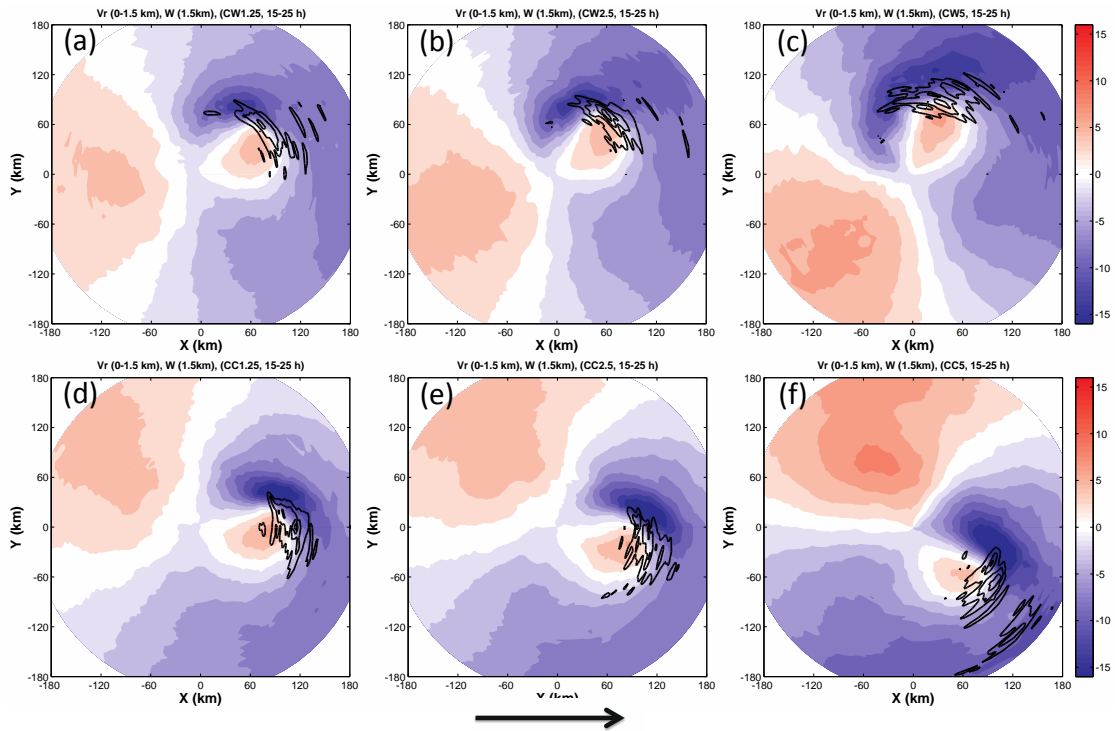
819 vertical acceleration ( $\text{m s}^{-2}$ ); (b and e) effective buoyancy acceleration ( $\text{m s}^{-2}$ ); and (c

820 and f) total vertical acceleration ( $\text{m s}^{-2}$ ). Black contours (from  $1 \text{ m s}^{-1}$  to  $4 \text{ m s}^{-1}$  with  $1$

821  $\text{m s}^{-1}$  interval) indicate vertical motion. The domain is chosen to ensure that the

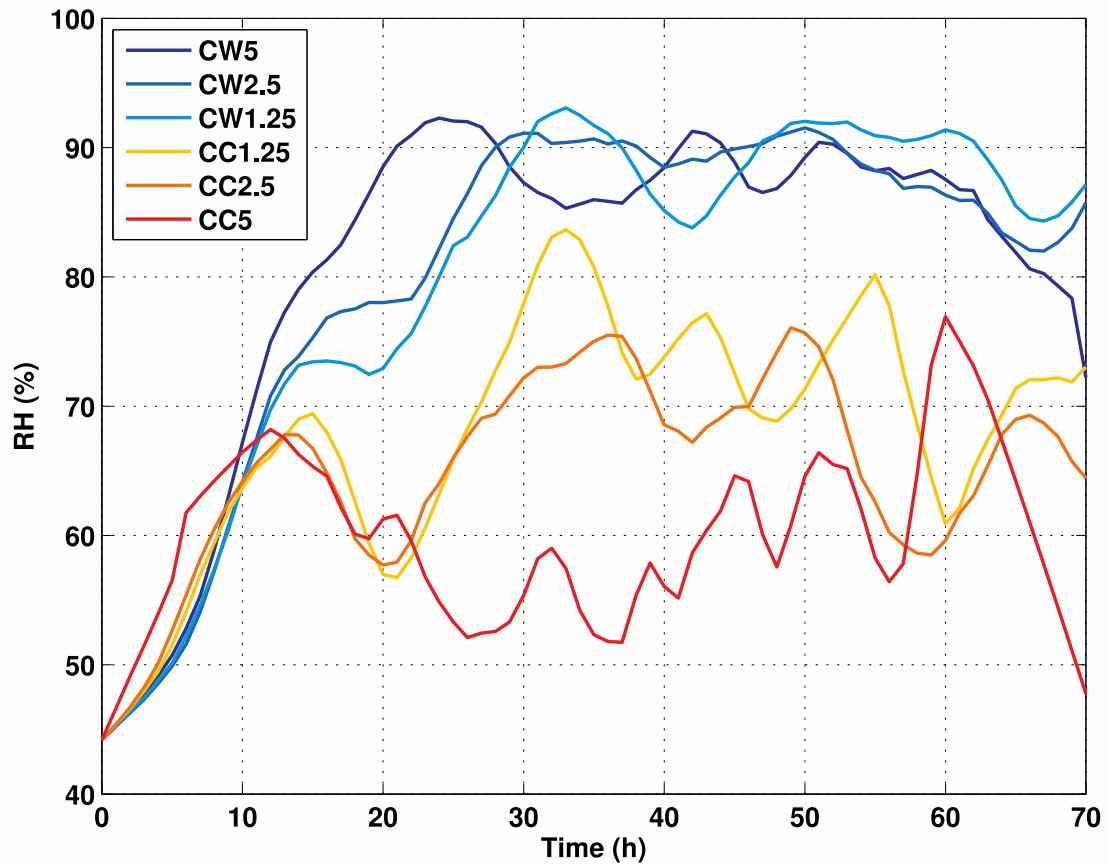
822 convection is near the center of the plot.

823



824  
825

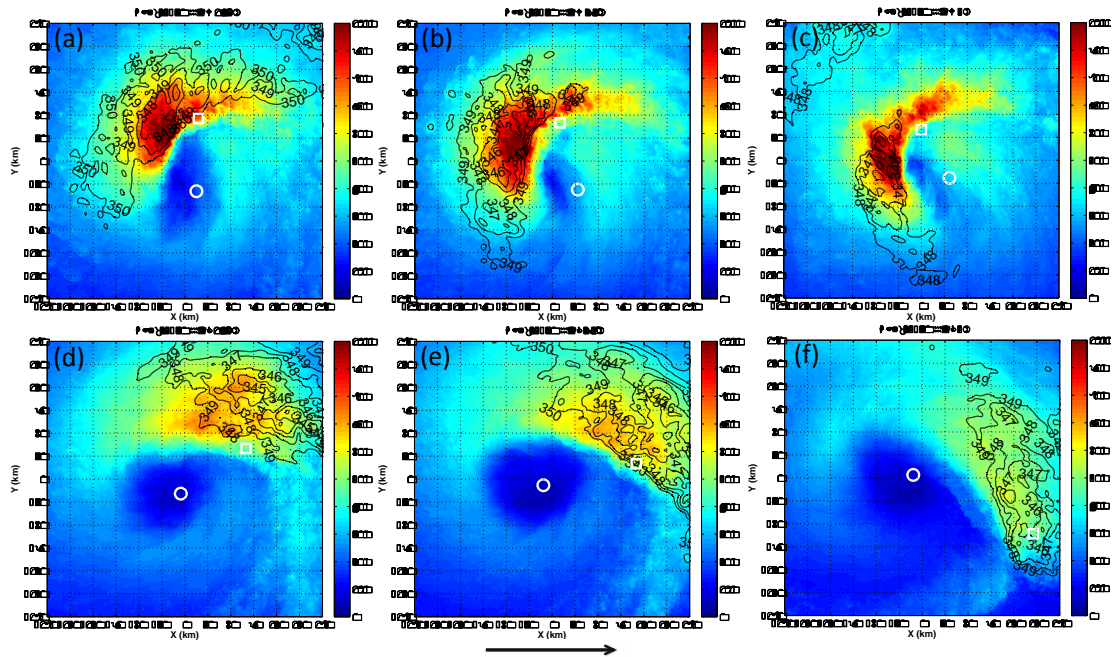
**FIG. 8.** Plane view of time averaged (15-25 h) radial velocity (shading;  $\text{m s}^{-1}$ ) within  
 826 the boundary layer (0-1.5 km) and time averaged (15-25 h) positive vertical velocity  
 827 (contours;  $\text{m s}^{-1}$ , every  $0.5 \text{ m s}^{-1}$  starting from  $0.5 \text{ m s}^{-1}$ ): (a) CW1.25, (b) CW2.5, (c)  
 828 CW5, (d) CC1.25, (e) CC2.5, and (f) CC5. The thick black arrow at the bottom of the  
 829 figure indicates the direction of deep-layer shear.



830

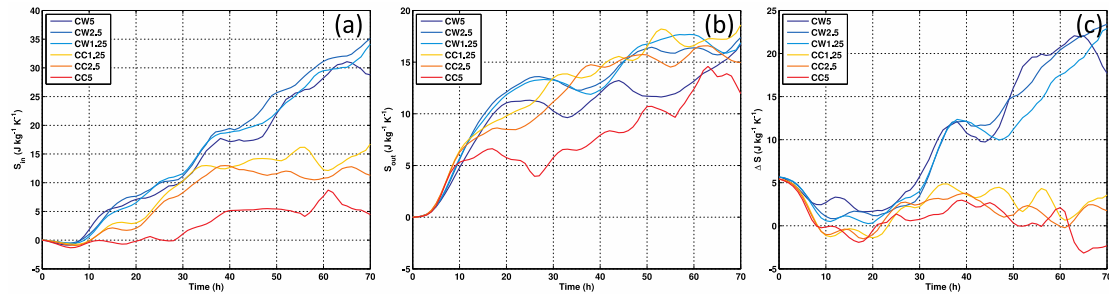
831 **FIG. 9.** Time evolution of relative humidity averaged over the mid-troposphere (4–8  
 832 km) for azimuth angles of  $30^\circ$  to  $60^\circ$  in the downstream region of overall vortex tilt and  
 833 within a radius of 30 to 150 km from the vortex center at a 2-km height in simulations  
 834 of directional shear flows. Line colors indicate the simulation: CC5 (red), CC2.5  
 835 (brown), CC1.25 (yellow), CW1.25 (light blue), CW2.5 (blue), and CW5 (dark blue).

836



837

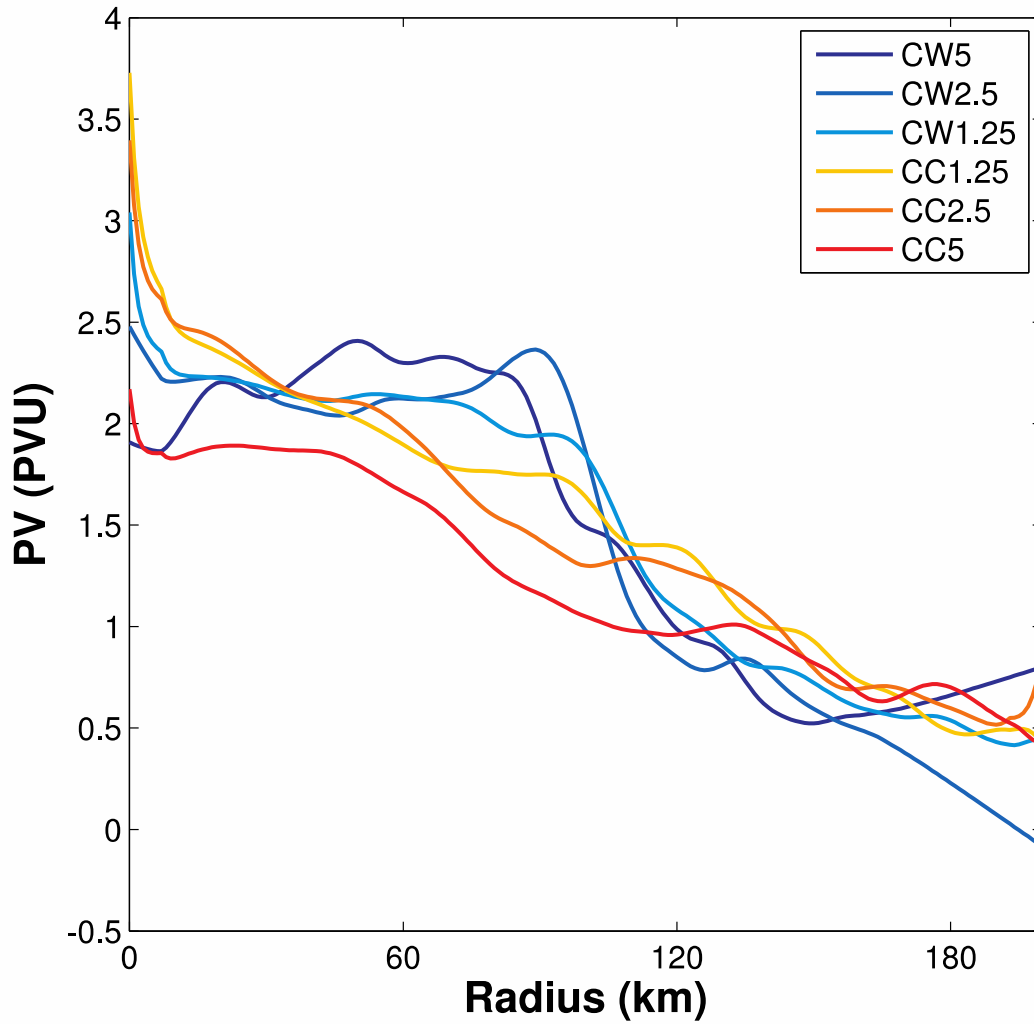
838 **FIG. 10.** As for Fig. 4, but for time-averaged surface heat flux (sum of latent heat flux  
 839 and sensible heat flux;  $\text{W m}^{-2}$ ) during hours 25–30. The white circle and square  
 840 represent the vortex centers at heights of 2 and 8 km at hour 30, respectively.



841

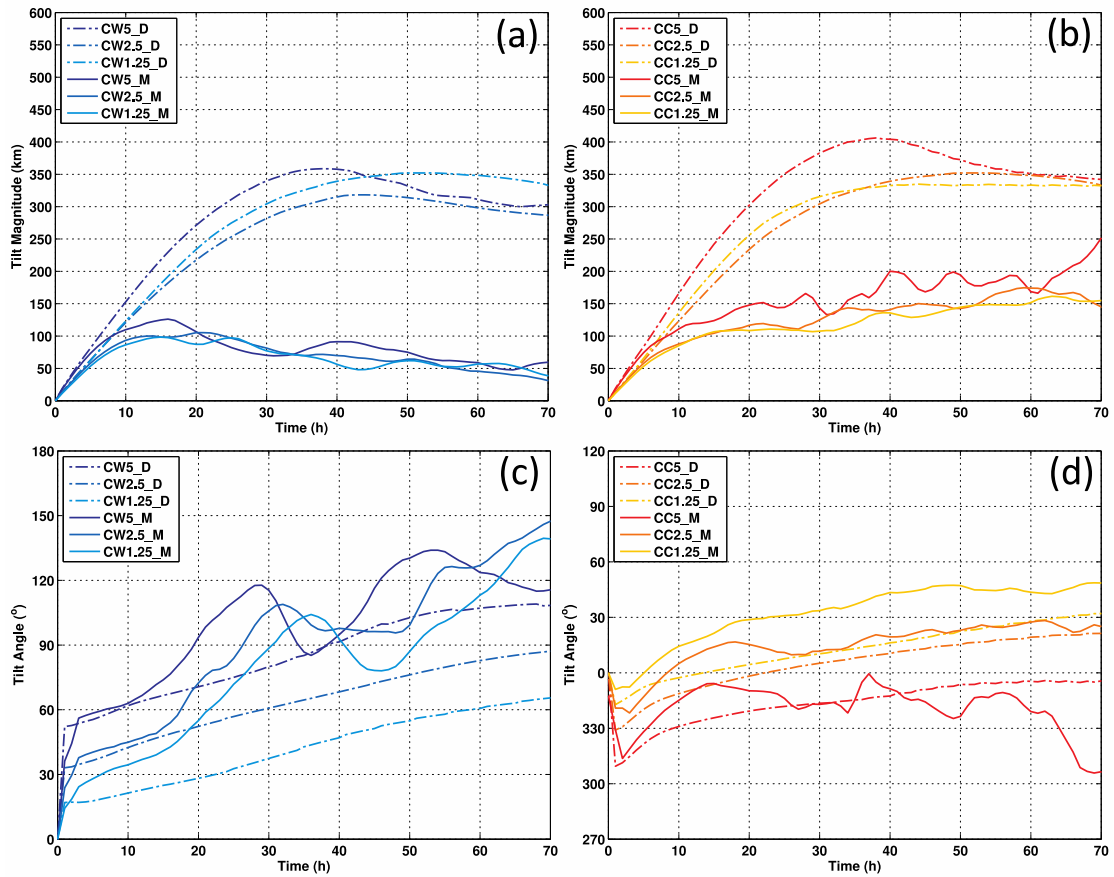
842 **FIG. 11.** Time evolution of azimuthally averaged moist entropy and moist entropy  
 843 difference between the inner- and outer-core regions over 4-8 km height: (a) moist  
 844 entropy in the inner region (0–80 km); (b) moist entropy in the outer region (100–180  
 845 km); (c) moist entropy difference between the inner and outer regions. Line colors  
 846 indicate the simulation: CC5 (red), CC2.5 (brown), CC1.25 (yellow), CW1.25 (light  
 847 blue), CW2.5 (blue), and CW5 (dark blue).

848



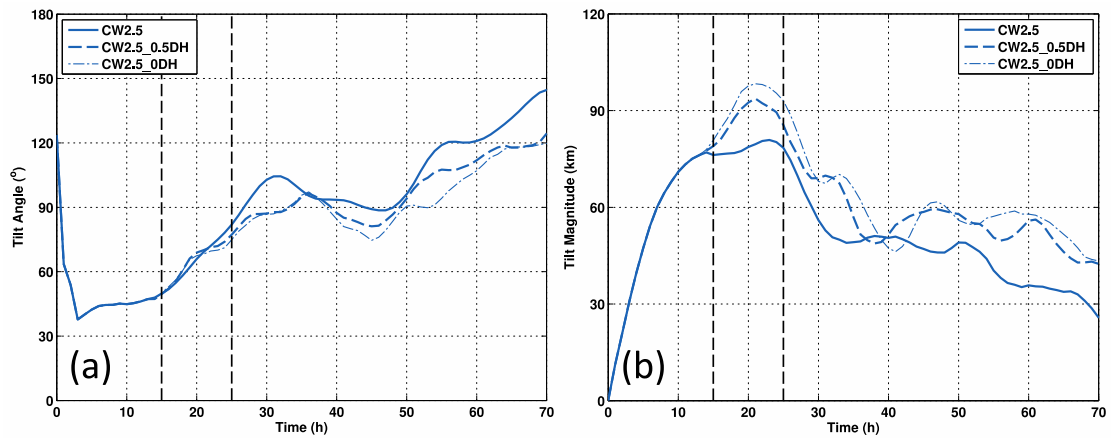
849

850 **FIG. 12.** Radial profile of azimuthally, vertically (2–5 km), and time-averaged (20–25  
 851 h) potential vorticity (PV). Line colors indicate the simulation: CC5 (red), CC2.5  
 852 (brown), CC1.25 (yellow), CW1.25 (light blue), CW2.5 (blue), and CW5 (dark blue).



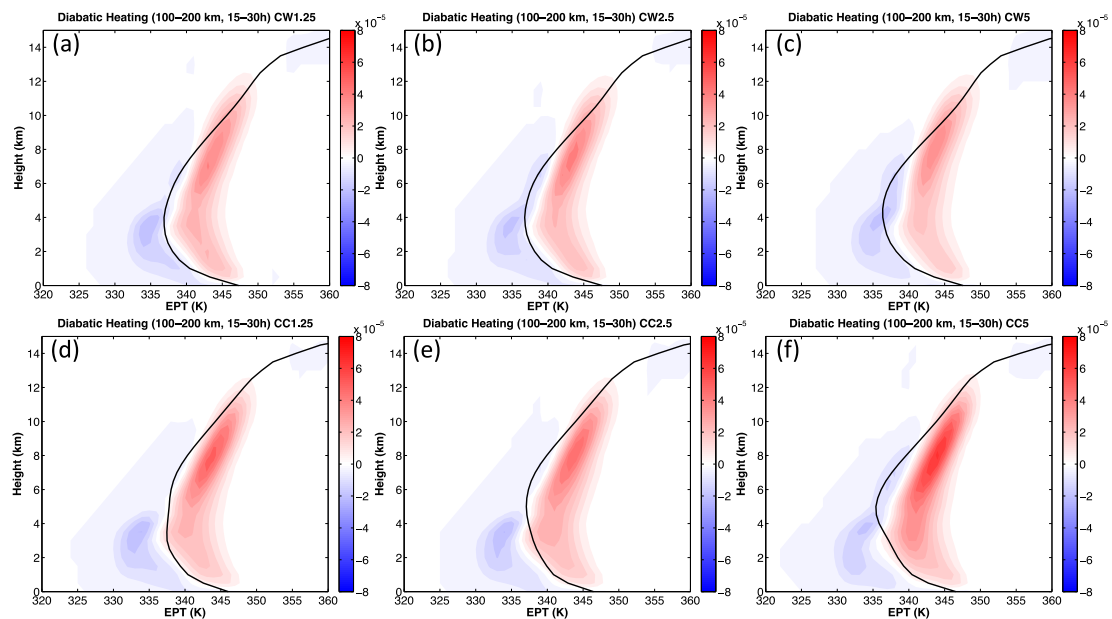
853

854 **FIG. 13.** Time evolution of overall vortex tilt (0–8 km) magnitude (km; a and b) and  
 855 tilt direction (degrees; c and d) for moist (solid line) and dry (dash–dotted line)  
 856 simulations: (a) tilt magnitude in CW hodographs; (b) tilt magnitude in CC hodographs;  
 857 (c) tilt direction in CW hodographs; and (d) tilt direction in CC hodographs. The tilt  
 858 angle is calculated counterclockwise from east (i.e.,  $0^\circ$  for east,  $90^\circ$  for north,  $180^\circ$  for  
 859 west, and  $270^\circ$  for south). The suffix ‘\_D’ denotes results from dry simulations and  
 860 ‘\_M’ denotes results from the corresponding moist simulations.



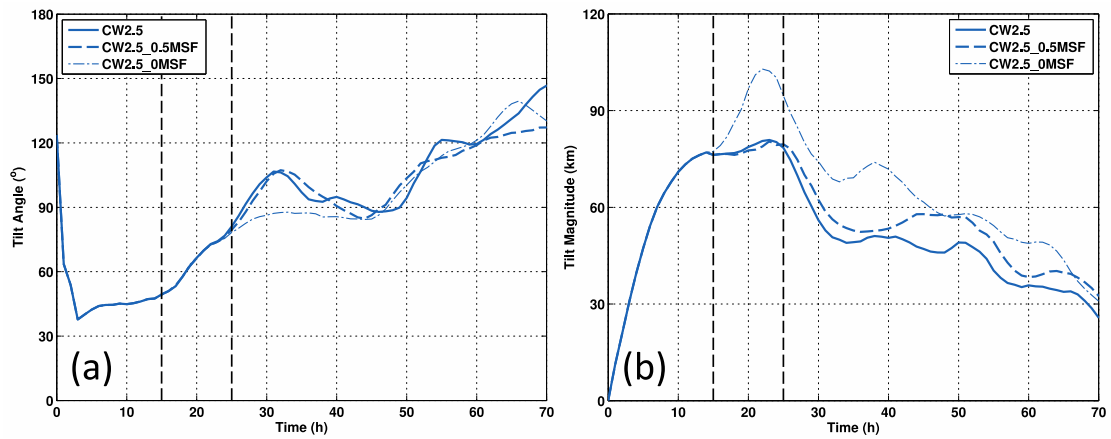
861

862 **FIG. 14.** Time evolution of overall vortex tilt (0–8 km) direction (degrees; a) and  
 863 magnitude (km; b) for CW2.5 (blue solid) and the latent heating sensitivity simulations  
 864 of CW2.5; i.e., CW2.5\_0.5DH (blue dashed) and CW2.5\_0DH (blue dashed–dotted).  
 865 The two black vertical dashed lines denote the timings at which the deactivation of  
 866 diabolic heating begins (15 h) and ends (25 h).



867

868 **FIG. 15.** Isentropic distribution of time-averaged (hours 15–30) diabatic heating ( $\text{K s}^{-1}$ )  
 869  $^1$ ) within 100–200 km of the vortex center at 2-km height: (a) CW1.25, (b) CW2.5, (c)  
 870 CW5, (d) CC1.25, (e) CC2.5, and (f) CC5. The abscissa is the equivalent potential  
 871 temperature (EPT). The black solid line represents the domain-averaged vertical profile  
 872 of equivalent potential temperature.



873

874 **FIG. 16.** Time evolution of overall vortex tilt (0–8 km) direction (degrees; a) and  
 875 magnitude (km; b) for CW2.5 (blue solid) and the surface heat flux sensitivity  
 876 simulations of CW2.5; i.e., CW2.5\_0.5MSF (blue dash) and CW2.5\_0MSF (blue  
 877 dashed–dotted). The two black vertical dashed lines denote the timings at which the  
 878 deactivation of surface heat fluxes begins (15 h) and ends (25 h).